INFLUENCE OF DIFFERENTIAL ROTATION AND PRECOLLAPSE ANGULAR MOMENTUM DISTRIBUTION ON STELLAR COLLAPSE AND ITS GRAVITATIONAL WAVE SIGNATURE

Final Report

Alexandra M. DeMaio,[1,2] Ernazar Abdikamalov (Adv.),[2] and Christian D. Ott (Adv.)[2,3]

[1]*Department of Physics and Astronomy, Rutgers, The State University of New Jersey, 136 Frelinghuysen Road Piscataway, NJ 08854-8019, USA*

[2]*TAPIR, MC 350-17, California Institute of Technology, 1200 E California Blvd., Pasadena, CA 91125, USA**

[3]*Kavli IPMU (WPI), University of Tokyo, Kashiwa, Japan 277-8583*

(Dated: September 27, 2013)

Core-collapse supernovae (CCSN) are theorized to produce gravitational waves that can be detected by observatories such as Advanced LIGO. We present results from detailed 2D, axisymmetric, equatorially symmetric, general relativistic simulations of core-collapse supernovae in the bounce and post-bounce phases, investigating the effects of precollapse differential rotation and central angular velocity on post-bounce stellar dynamics and gravitational wave signals. We conclude that the distribution of angular momentum is detectable primarily in CCSN from rapidly rotating progenitor stars. We employ matched filtering and Bayesian analysis with principle component decomposition to determine the potency of observed disparities among the model waveforms.

I. BACKGROUND

The life cycles of massive stars ($8M_\odot \lesssim M \lesssim 130M_\odot$ at zero-age main-sequence) typically end in core-collapse supernovae (CCSN). All stars form progressively heavier elements via nuclear burning, but only sufficiently massive stars are capable of sustaining the temperatures necessary to form iron cores. Because iron is the most efficiently bound element, its fusion is energetically disfavored. As fusion ceases, the gravitational self-attraction of the core grows to rival electron degeneracy pressure. When the core is so massive that the two forces are equal (at the Chandrasekhar mass), rapid collapse begins. The density of the core increases until the equation of state stiffens at nuclear saturation density, at which point the inner core rebounds (bounces), producing a shockwave. Heavy ions from the still infalling outer core resist the shockwave. Their dissociation, in combination with neutrino emission from behind the shock front, dissipates energy and causes the shock to stall, thus a shock revival mechanism is necessary to produce the ultimate supernova explosion [1].

Shock revival is one of many poorly understood features of supernovae. The nuclear equation of state, the distribution of angular momentum in progenitor stars, and other open topics are studied through the analysis of rotational dynamics in CCSN. To understand the evolution of supernovae, it is imperative to analyze the dynamics of the stellar inner core, which is the metaphorical "engine" of supernova events. Traditional astrophysical probes such as electromagnetic waves and nucelosynthesis products are inadequate in this respect. Electromagnetic waves are produced in the photosphere - too far outside the inner core to probe its properties accurately; nucleosynthesis products sometimes originate from the inner core, but they become available to analyze only substantially after they are relevant to understanding phenomena such as shock revival.

Gravitational wave analysis is a promising supplement to current methods. In the framework of general relativity, gravitational waves are expected from accelerated mass-quadrupole moments (and higher-order moments), which are produced in the inner core during collapse and bounce. Because they are produced in the stellar region of interest and their signals are negligibly changed as they travel to Earth, gravitational waves are anticipated to be excellent probes of inner-core dynamics. Although gravitational waves have not yet been observed directly, detectors such as Advanced LIGO are currently being calibrated to collect data within the next few years [2].

Herein, we study the gravitational wave signature produced due to centrifugally deformed collapse, bounce, and ring-down oscillations in rapidly rotating stars. Predictions about the gravitational waves produced in CCSN must integrate all of the processes involved in the hydrodynamic evolution of stars, which includes a broad spectrum of precollapse parameters [1]. Because analytical derivations of these relationships would require detailed calculations of turbulence in MHD, extensive parameter studies are necessary to broaden and refine current information. The purpose of this study is to assess the effects of precollapse differential rotation and central angular velocity on the dynamics of CCSN and the gravitational waves they produce. We expand on several previous parameter studies, performing 124 simulations of rotating

*Electronic address: alexandra.demaio@rutgers.edu

core collapse and bounce in progenitors with differing central angular velocities and differential rotation.

The following information is directly from [3].

II. INTRODUCTION

Massive stars ($8M_\odot \lesssim M \lesssim 130M_\odot$ at zero age main sequence [ZAMS]) undergo collapse at the end of their nuclear burning lifes once their electron-degenerate core exceeds its effective Chandrasekhar mass. The inner core collapses subsonically and once its density exceeds that of nuclear matter, experiences core bounce due to the stiffening of the nuclear equation of state (EOS). A hydrodynamic bounce shock forms at the interface of inner and supersonically collapsing outer core. The shock quickly moves out, but stalls within a few tens of milliseconds and at a radius of $100 - 200\,\mathrm{km}$ due to dissociation of infalling iron-group nuclei and energy losses to neutrinos that stream away from the semi-transparent region behind the shock [4]. The shock must be revived by some mechanism to drive an explosion and create the spectacular display of a core-collapse supernova across the electromagnetic spectrum.

For the vast majority of core-collapse supernovae with explosion energies of $\sim 0.1 - 1\,\mathrm{B}$ ($1\mathrm{B}ethe = 10^{51}\,\mathrm{erg}$) the *neutrino mechanism* [5–7] is the favored mechanism of shock revival. It relies on the deposition of a fraction of the outgoing electron neutrino and electron antineutrino luminosity (with a typical efficiency of order 10%) behind the stalled shock, but also requires neutrino-driven convection and/or the standing accretion shock instability (SASI; e.g., [8]) to increase the dwell time of accreted matter in the region behind the shock where net energy absorption is possible. The neutrino mechanism fails in spherical symmetry (1D, where convection and SASI are absent). A number of axisymmetric (2D) core-collapse supernova simulations with detailed energy-dependent neutrino transport and microphysics now report successful explosions [9–11], but first such 3D simulations are not yet conclusive [12, 13].

There is, however, a class of highly-energetic core-collapse supernovae with inferred explosion energies of up to 10 B that the neutrino mechanism alone seems too feeble to possibly explain. This class includes relativistic Type Ic supernovae with strongly Doppler-broadened spectral lines from compact hydrogen/helium-poor progenitors (so called Type Ic-bl SNe; e.g. [14, 15]) and super-energetic Type II supernovae from red supergiants (e.g., [16, 17]) and makes up 1-2% of all core-collapse supernovae [15]. All supernovae associated with long gamma-ray bursts have been of Type Ic-bl [18, 19].

Such energetic events may require a central engine that can convert the gravitational energy provided by collapse much more efficiently into energy of the explosive outflow than neutrinos are capable of. One possibility is the *magnetorotational mechanism* in which a millisecond-period protoneutron star with magnetar-strength magnetic fields drives a jet-driven bipolar explosion [20–24], which, in some cases, might set the stage for a subsequent long gamma-ray burst (e.g., [25, 26]).

Current standard lore of stellar evolution theory and pulsar birth-spin estimates have it that most massive stars are rather slow rotators at the end of their lives, having lost angular momentum to stellar winds and being not strongly differentially rotating due to angular-momentum redistribution by magnetic torques (e.g., [27, 28]). Special conditions such as chemically homogeneous evolution at low metallicity [29, 30] or binary interactions [31] might be necessary to produce the progenitors of hyper-energetic core-collapse supernovae and long GRBs.

This may or may not be the case. Current stellar evolutionary calculations are still 1D and take into account rotation and angular momentum loss and redistribution only approximately and in a parameterized, not self-consistent way. Pulsar birth-spin estimates, which are based on magnetic-dipole radiation, could be off by large factors if early spin-down occurred by direct conversion of spin energy into magnetic field and/or kinetic energy of an explosive outflow. Keeping this in mind, it is not inconceivable that rotation could play a significant role in many core-collapse supernovae. Rotating core collapse naturally leads to differential rotation in the outer protoneutron star and in the postshock region [28, 32]. The free energy in differential rotation[1] could be tapped by the magnetorotational instability (e.g., [33–35]), which could either lead to the growth of large-scale magnetic field (as argued for by [24, 35]) or local dissipation (and additional heating) by reconnection [36]. Depending on precollapse spin and magnetization, both possibilities could either subdominantly assist the neutrino mechanism in reviving the shock or dominate the dynamics in a magnetorotational [24] or magneto-viscous [36, 37] explosion.

Gravitational waves (GWs) are the most direct and best probes of rotation in stellar collapse and core-collapse supernovae. Rotation naturally leads to a quadrupole (i.e. oblate) deformation of the collapsing

[1] At fixed total angular momentum, uniform rotation is the lowest energy state. Any process capable of redistributing angular momentum will operate on differential rotation, driving a system towards uniform rotation.

core. The centrifugally-deformed core undergoes extreme accelerations during the late collapse, bounce, and early postbounce phase. This provides an extremely large accelerated quadrupole moment, resulting in a GW burst signal that, depending on the amount of angular momentum in the inner core, can be detected by the upcoming advanced-generation of GW detectors out to $10-100\,\mathrm{kpc}$ [38–40]. After core bounce, on a timescale of tens of milliseconds, non-axisymmetric dynamics may develop due to rotational shear instabilities (e.g., [41–43]), leading to longer-term quasi-periodic GW emission.

Much effort has gone into modeling the GW signal from rotating core collapse and bounce over the past three decades [1, 38, 39, 41, 44–53] and the current state of the art is set by simulations in conformally-flat or full general relativity (GR) that include realistic EOS and approximate neutrino transport [38–40, 43]. These studies found that the GW signal from rapidly rotating core collapse and bounce has rather simple morphology and can be described by a prebounce rise in GW strain h, a large spike at bounce, and a subsequent postbounce ring-down phase in which the protoneutron star hydrodynamically dissipates its remaining pulsational energy from bounce. Simulations that included magnetic fields showed that the bounce and very early postbounce phase and the associated GW signal are not affected by magnetohydrodynamic effects unless the precollapse seed fields are unrealistically large ($B \gtrsim 10^{12}$) [53–57]. Dimmelmeier *et al.* [38] and Abdikamalov *et al.* [40] showed that the peak GW strain from collapse and bounce depends primarily and sensitively on the mass and angular momentum of the inner core at bounce. Dimmelmeier *et al.* [38], who considered two finite-temperature nuclear EOS, the EOS of H. Shen *et al.* [58, 59] and the Lattimer-Swesty EOS [60], found only a weak dependence of the GW signal on the nuclear EOS. Ott *et al.* [39] recently showed that in rapidly rotating cores that make protoneutron stars with spin periods $\lesssim 5\,\mathrm{ms}$, the GW signal depends on the precollapse angular momentum of the core, but not its detailed structure and progenitor ZAMS mass. Furthermore, they demonstrated that postbounce neutrino emission has little influence on the GW signal from bounce and ring-down.

In this work, we extend previous work and focus on the influence of the angular momentum distribution in the progenitor core on the GW signal of rotating core collapse, bounce, and ring-down. To this end, we carry out 124 simulations with the axisymmetric GR core-collapse code `COCONUT` [40, 61, 62]. We employ the Lattimer-Swesty $K = 220\,\mathrm{MeV}$ EOS [60] and treat electron capture during collapse with the deleptonization scheme of [38, 63]. After bounce, we employ the neutrino-leakage scheme used in [39]. Motivated by the findings of [39], we consider only a single progenitor model (the 12-$M_\odot$ [at ZAMS] solar-metallicity progenitor of [64]) and carry out a systematic set of simulations with five different degrees of differential rotation and a fine-grained grid of initial central angular velocities. In order to investigate the dependence of our results on the details of EOS and deleptonization scheme, we repeat a select subset of our models with the Shen *et al.* [58, 65] EOS and a modified deleptonization scheme.

The results of our simulations show that the GW signal of rapidly rotating cores has a strong and systematic dependence on the precollapse degree of differential rotation. This is true for cores that collapse to rapidly rotating protoneutron stars with ratio of rotational kinetic energy to gravitational energy $\beta = T/|W| \gtrsim 0.05$. The GW signal of more slowly spinning cores has little dependence on differential rotation and instead just depends on the cores "total rotation," parameterized by its $\beta = T/|W|$ at core bounce. We supplement our simulation results with a matched-filtering analysis and by a Bayesian model selection analysis motivated by [66]. Assuming Advanced LIGO (aLIGO; [67]) design sensitivity, we demonstrate that it is possible to measure total rotation (i.e. β) with $\sim$10% accuracy for unknown injected rotating core collapse signals. We also show that the degree of differential rotation can be estimated, but robustly only for rapidly rotating models and if the EOS is known.

This paper is organized as follows. In Section III, we describe our computational code and in Section IV, we discuss our precollapse configurations. Section V presents the results of our core collapse simulations and analyzes the effects of differential rotation on dynamics and GW signal. In Section VI, we present the matched-filtering analysis and Bayesian model selection results. We summarize and conclude in Section VII.

III. METHODS

We perform our simulation in axisymmetric (2D) conformally-flat GR with the `CoCoNuT` code, which has been extensively described in [1, 38, 40, 62]. The conformal-flatness condition (CFC) has been shown to be an excellent approximation to full GR in the context of rotating stellar collapse to protoneutron stars [41]. `CoCoNuT` employs Eulerian spherical coordinates and solves the non-linear elliptic CFC equations using spectral methods [62]. GR hydrodynamics is implemented following the Valencia formulation [68] via a finite-volume method with piecewise parabolic reconstruction [69], and the approximate HLLE Riemann solver [70]. The version of `CoCoNuT` used here is the same as in [40], but we have upgraded the EOS and neutrino microphysics routines as described in the following.

We use the tabulated, finite-temperature nuclear EOS by Lattimer & Swesty [60] with $K = 220\,\mathrm{MeV}$ generated by [71] and available for download from `stellarcollapse.org`. More information on this EOS and the details of its implementation in a tabulated form can be found in [71, 72]. In order to study the effect of the nuclear EOS itself, we repeat a select set of our models with the Shen *et al.* [58, 65] EOS.

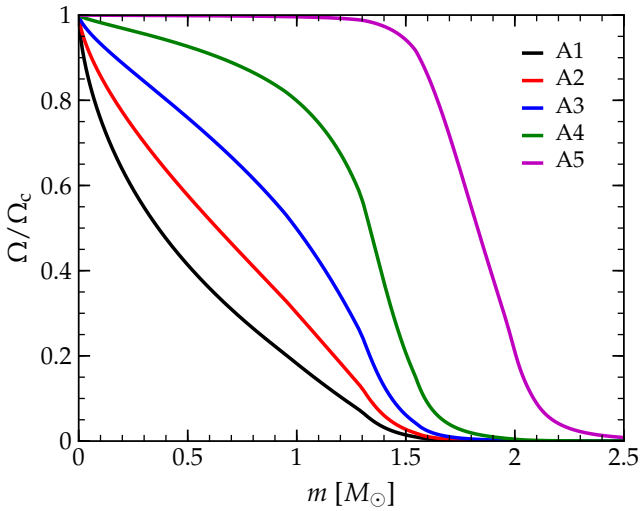

FIG. 1: The ratio of the angular velocity to the central angular velocity as a function of the enclosed-mass coordinate along the equatorial plane for the s12WH07 progenitor for the five different values of the differential rotation parameter A considered in this study (cf. Table I).

We employ the neutrino microphysics routines provided by the open-source code `GR1D` [71, 73, 74], also available for download from `stellarcollapse.org`. During the collapse phase, we use the parameterized $Y_e(\rho)$ deleptonization scheme [75] with the same parameters used in [39]. In the postbounce phase, we use the neutrino leakage/heating scheme of [71] to approximate deleptonization as well as neutrino cooling and heating. We implement the optical depth calculation along radial rays aligned with `CoCoNuT`'s radial zones and use the default heating scaling factor $f_{\rm heat} = 1$ of this scheme. This leakage/heating scheme has also been applied in the multi-dimensional simulations of [39, 76].

As in previous studies (e.g., [38, 40]), we perform our simulations in a spherical domain spanning 3000 km in radius under the assumption of equatorial symmetry. In our production simulations, we cover our domain with 250 logarithmically spaced radial grids with a central resolution of 250 m. The 90° of our domain are covered with 40 equidistant angular grid points. We have performed a resolution study to ensure that this resolution is sufficient for the purpose of this study.

We extract GWs using the variant of the Newtonian quadrupole formula given in [62], which is very accurate in the case of rotating stellar collapse to protoneutron stars [77].

IV. INITIAL MODELS

Existing presupernova stellar models with rotation are evolved using spherically-symmetric codes assuming shellular rotation (*e.g.*, [27, 29, 78]). In these models, the key processes that determine the precollapse rotational configuration such as the magnetic braking [*e.g.*, 79] and mass loss [*e.g.*, 80] are treated only approximately, while the potentially important effects of binary interactions [*e.g.*, 31] are generally not included at all.

Since our knowledge of the precollapse rotational configuration is far from being certain, we employ the nonrotating 12-$M_\odot$ solar-metallicity progenitor model of [64] (model s12WH07) and impose a simple parametrized rotation profile, which facilitates control of the total angular momentum and its distribution. We use the cylindrical rotation law of [47, 50],

$$\Omega(\varpi) = \Omega_{\rm c}\left[1+\left(\frac{\varpi}{A}\right)^2\right]^{-1}\ , \qquad (1)$$

where $\Omega_{\rm c}$ is the initial central angular velocity, ϖ is the cylindrical radius, and A is the parameter that controls the degree of differential rotation. This rotation law yields constant specific angular momentum at $\varpi \gg A$. Upon mapping into the code, the spherically symmetric initial model is set into rotation according to Eq. (1). Collapse proceeds more slowly than the sound crossing time of the core and the latter is quickly driven into an oblate shape by centrifugal effects. The validity of this approach was studied by [47].

It is important to note that it is currently unclear how realistic the rotation law given by Eq. (1) truly is. However, this is not a concern for our work, since we aim to explore if and how different angular momentum distributions affect the GW signature of rotating core collapse, bounce, and early postbounce dynamics. For that purpose, we need a rotation law that (*i*) roughly reproduces the angular momentum distribution expected in stellar cores[2], (*ii*) does not violate any known physical principles and constraints that are relevant in the regime with which we are concerned, and (*iii*) allows us to easily construct models with different amounts and distributions of angular momentum. The rotation law given by Eq. (1) fulfills these requirements.

We restrict our analysis to a single progenitor model since different models with the same distribution of angular momentum as a function of enclosed mass are likely to produce very similar dynamics and GW signals at bounce and in the early postbounce ring-down phase. This was demonstrated by [39].

We consider five sets of models with five different values of the differential rotation parameter A: $A1 = 300\,$km, $A2 = 417\,$km, $A3 = 634\,$km, $A4 = 1268\,$km, and $A5 = 10000\,$km. Figure 1 depicts the ratio $\Omega/\Omega_{\rm c}$ as a function of mass coordinate for these values of A in the s12WH07 progenitor model. The higher the value of A, the weaker the differential rotation. The specific choices

[2] The rotation law given by Eq. (1) reproduces the radial angular momentum distribution in, *e.g.*, rapidly rotating models 16TI and 16OM of Woosley & Heger [29] with reasonable accuracy in the inner $\sim 2M_\odot$ for $A \sim 850$ km.

of the Ai are motivated as follows: $A3$ is the same value used in [39] and gives an angular velocity at a mass coordinate of $1\,M_\odot$ that is one half of the central value. $A4$ is twice as large as $A3$, allowing us to probe somewhat more rigid initial rotation, and $A5$ ensures near uniform rotation in the inner $1.5\,M_\odot$ (corresponding to a radius of $\sim 3\times10^3$ km). $A1$ corresponds to extremely differential rotation and $A2$ is in the middle between $A1$ and $A3$.

For each choice of A, we simulate sequences of models with initial central angular velocities starting at $\Omega_{\rm c,min} = 1\,{\rm rad\,s^{-1}}$ (for this value, rotation is dynamically insignificant in all models). We increase in $\Omega_{\rm c}$ steps of $0.5\,{\rm rad\,s^{-1}}$. In models with weak or moderate differential rotation (sequences $A3-A5$), the maximum initial central angular velocity $\Omega_{\rm c,max}$ is set by the value at which such models still collapse. For more differentially rotating models, we choose $\Omega_{\rm c,max}$ in such a way that we obtain the global maximum of $\beta_{\rm ic,b} = (T/|W|)_{\rm ic,b}$, the ratio of rotational kinetic energy to gravitational energy of the inner core at bounce. We compute $T/|W|$ via the definition given by [81] and focus on the inner core, because the bounce dynamics and the associated GW signal are determined by its spin and mass [38, 40]. Note that models with $\Omega_{\rm c} > \Omega_{\rm c,max}$ yield decreasing $\beta_{\rm ic,b}$ (see, e.g., the discussions in [28, 38, 50]). Since such models collapse only in the case of very strong differential rotation, they are not useful for our goal of comparing different degrees of differential rotation.

V. RESULTS: DYNAMICS AND WAVEFORMS

The top panel of Fig. 2 depicts the time evolution of the central density $\rho_{\rm c}$ during the last phase of collapse, bounce, and the early postbounce phase of model A3O6, which is representative for many of the simulated models. For future reference, we define the *time of core bounce* as the moment at which the specific entropy at the edge of the inner core in the equatorial plane reaches $3\,k_{\rm B}\,{\rm baryon}^{-1}$. Just before bounce, $\rho_{\rm c}$ increases rapidly due to the accelerated contraction of the inner core. Once nuclear density is reached, the stiffening of the nuclear EOS abruptly decelerates collapse. The inner core overshoots its equilibrium configuration due to its immense inertia and consequently $\rho_{\rm c}$ reaches $\sim 3.7\times10^{14}\,{\rm g\,cm^{-3}}$ at maximum contraction. The core bounces back and settles at a postbounce (pb) quasi-equilibrium central density $\rho_{\rm c,pb}$ of $\sim 3\times10^{14}\,{\rm g\,cm^{-3}}$, after a series of ring-down oscillations that last for $\sim 10-15$ ms. These oscillations are clearly visible in the evolution of the central density in the postbounce phase as a quasi-periodic $\sim 7\,\%$ variation of $\rho_{\rm c}$.

The middle panel of Fig. 2 shows $\beta = T/|W|$ of the inner core for model A3O6. By construction, β directly reflects the importance of rotational support in gravitationally bound objects [82]. Much like $\rho_{\rm c}$, $\beta_{\rm ic}$ grows in the final phase of collapse due to the spin-up of the inner core, as a consequence of angular momentum conservation. At bounce, $\beta_{\rm ic}$ peaks at ~ 0.1 in this model, before decreasing to ~ 0.08 while the inner core settles into its postbounce quasi-equilibrium. The ring-down protoneutron star oscillations in the postbounce phase are also visible as small variations in $\beta_{\rm ic}$.

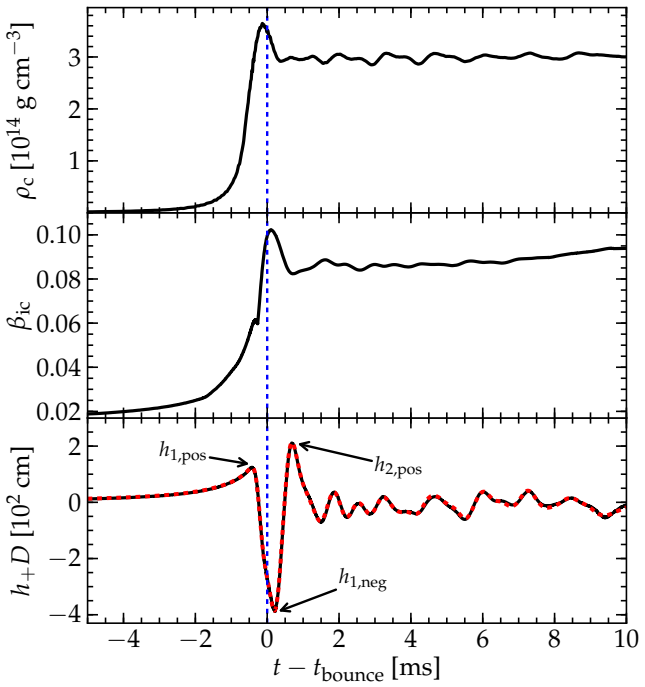

FIG. 2: Time evolution of the central density (top panel), $\beta_{\rm ic}$ (center panel), and GW strain (bottom panel; rescaled by source distance D) in model A3O6. The arrows indicate the first three pronounced generic features of the GW signal, labeled $h_{1,\rm pos}$, $h_{1,\rm neg}$, and $h_{2,\rm pos}$. The thin vertical dashed line indicates the time of core bounce defined as the time at which the equatorial edge of the inner core reaches an entropy of $3\,k_{\rm B}\,{\rm baryon}^{-1}$. The dashed red line shows the GW strain for the same model simulated with 50 % higher resolution in both the angular and radial direction. There is excellent agreement, which suggests that our fiducial resolution results in convergence.

In Fig. 3, we show $\beta_{\rm ic,b}$ as a function of the initial central angular velocity $\Omega_{\rm c}$ for all models used. At fixed $\Omega_{\rm c}$, strongly differentially rotating models reach smaller $\beta_{\rm ic,b}$, due to the comparatively modest total angular momenta in their inner cores, relative to more weakly differentially rotating models. Uniformly and mildly differentially rotating models (sequences $A3-A5$) eventually become fully centrifugally supported at the start of the simulations with increasing $\Omega_{\rm c}$, such that they do not collapse.

Due to this, the graphs in Fig. 3 for such models terminate at small to moderate Ω_c, and the corresponding maximum $\beta_{\rm ic,b}$ reached for sequences $A5$, $A4$ and $A3$ are 0.11, 0.13, and 0.18 respectively.

More strongly differentially rotating models, however, collapse even at high Ω_c. Sequences $A2$ and $A1$ reach $\beta_{\rm ic,b}$ of 0.19 and 0.21, respectively. The graphs corre-

Model sequence	A [km]	$\Omega_{\rm c,min}$ [rad s^{-1}]	$\Omega_{\rm c,max}$ [rad s^{-1}]	$\beta_{\rm ic,b,min}$ [10^{-2}]	$\beta_{\rm ic,b,max}$	Number of models
$A1$	300	1	15.5	1.62	0.21	30
$A2$	417	1	11.5	3.13	0.19	22
$A3$	634	1	9.5	3.58	0.18	18
$A4$	1268	1	6.5	4.66	0.13	12
$A5$	10000	1	5.5	5.15	0.11	10

TABLE I: Summary of key parameters of each model sequence. $\Omega_{\rm c,max}$ is the central angular velocity corresponding to the fastest model in each A-sequence, respectively. $\beta_{\rm ic,b,min}$ and $\beta_{\rm ic,b,max}$ are the values of $\beta = T/|W|$ of the inner core at bounce for the slowest and fastest rotators of each sequence, respectively. Note that $\Omega_{\rm c,max}$ and $\beta_{\rm ic,b,max}$ in the only mildly differentially rotating sequence $A4$ and $A5$ are limited by the fact that more rapidly spinning models fail to collapse. In more differentially rotating models, $\Omega_{\rm c,max}$ is the value for which we obtain $\beta_{\rm ic,b,max}$. Due to centrifugal effects, models with higher initial $\Omega_{\rm c}$ yield smaller $\beta_{\rm ic,b}$ (see, Fig. 4, and, e.g., [28, 38, 50]).

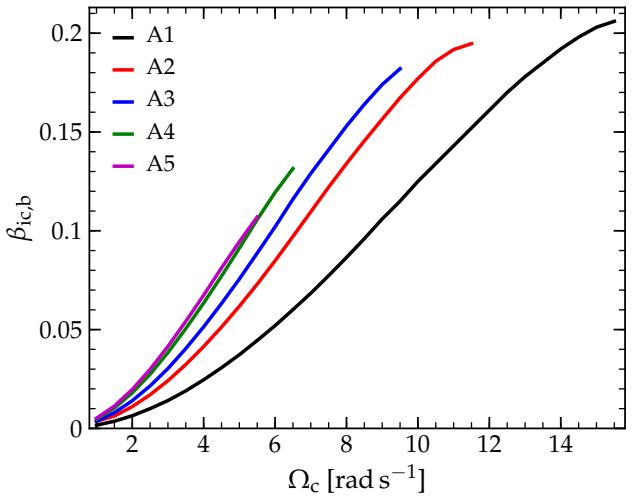

FIG. 3: Ratio of rotational kinetic energy to gravitational energy of the inner core at bounce $\beta_{\rm ic,b}$ as a function of initial central angular velocity $\Omega_{\rm c}$. All model sequences, from near uniform rotation ($A5$) to strong differential rotation ($A1$), are shown. Sequences with uniform or moderate differential rotation terminate at Ω_c beyond which they would be fully centrifugally supported already at the onset of collapse. Cf. Table I. Note that the mapping $\Omega_c \to \beta_{\rm ic,b}$ depends on progenitor structure [39].

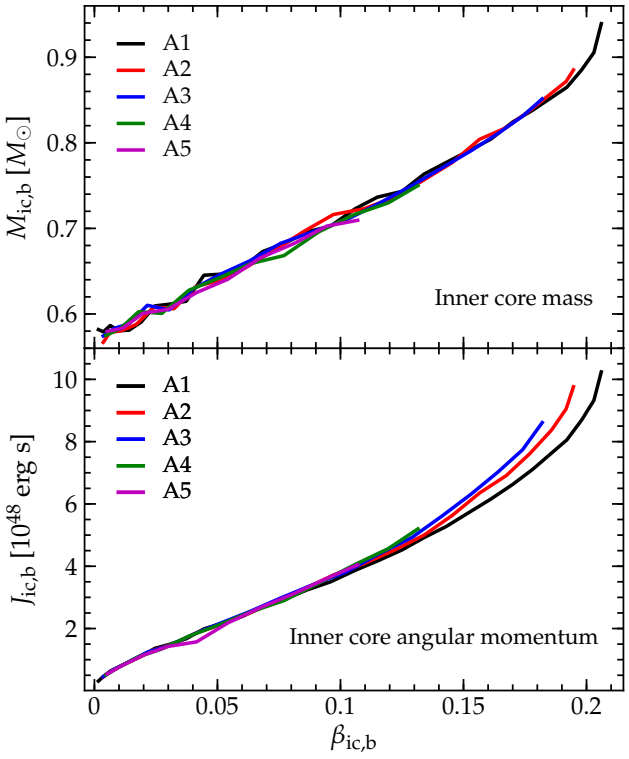

FIG. 4: Mass of the inner core at bounce ($M_{\rm ic,b}$, top panel) and angular momentum ($J_{\rm ic,b}$, bottom panel) as a function of $\beta_{\rm ic,b}$ for all model sequences, varying from near uniform rotation ($A5$) to strong differential rotation ($A1$). $J_{\rm ic,b}$ increases linearly with $\beta_{\rm ic,b}$ and, for $\beta_{\rm ic,b} \lesssim 0.12$, is nearly independent of the degree of differential rotation. $M_{\rm ic,b}$ also increases with $\beta_{\rm ic,b}$ (and $J_{\rm ic,b}$) and is essentially independent of differential rotation for $\beta_{\rm ic,b} \lesssim 0.18$.

sponding to these models in Fig. 3 show that these values are very close to the obtainable global maximum. A further increase in Ω_c would lead to a decrease in $\beta_{\rm ic,b}$, because bounce occurs centrifugally at lower core densities, corresponding to a smaller degree of spin-up (see the extensive discussions in [28, 40, 50]).

A. Influence of Differential Rotation on Collapse, Bounce and Early Postbounce Dynamics

The central objective of this work is to infer the effects of the angular momentum distribution in the progenitor core on the dynamics of core collapse, bounce, and the early ring-down oscillations. As demonstrated already in previous work (e.g., [38, 52]), the effect on the inner core is most important, since it's mass and angular momentum (and, perhaps, its distribution) determine the resulting GW signal. We will discuss the details of the latter in Section V B.

As a start, it is useful to define a quantity that de-

scribes the "total rotation" of the inner core. One possibility is to use the already introduced quantity $\beta_{\rm ic}$. It is most useful to consider the value of $\beta_{\rm ic}$ at bounce, since this is also the time at which the highest GW amplitudes occur. An obvious alternative choice is the total angular momentum of the inner core $J_{\rm ic}$, which, again, is best considered at the time of core bounce. Another alternative, though less direct measure is the mass of the unshocked inner core at bounce $M_{\rm ic,b}$. In the nonrotating case, $M_{\rm ic,b}$ is determined by the trapped lepton fraction in the inner core (e.g., [4]). Rotation increases $M_{\rm ic,b}$ by slowing down collapse and thus allowing a greater amount of material to be in sonic contact and part of the inner core [38, 40, 45].

Figure 4 shows that $\beta_{\rm ic,b}$, $J_{\rm ic,b}$, and $M_{\rm ic,b}$ obey a simple linear relationship and are independent of the degree of differential rotation through most of the considered model parameter space. Thus they can be used interchangeably to describe "total rotation". The simple relationship becomes non-linear and dependent on the differential rotation parameter A only for very rapid rotation ($\beta_{\rm ic,b} \gtrsim 0.15$, $J_{\rm ic,b} \gtrsim 6 \times 10^{48}\,{\rm erg\,s}$, $M_{\rm ic,b} \gtrsim 0.8\,M_\odot$).

The mapping $\beta_{\rm ic,b} \rightarrow J_{\rm ic,b}$, shown in the lower panel of Fig. 4, exhibits interesting dependence on A in rapidly rotating models with $\beta_{\rm ic,b} \gtrsim 0.13 - 0.15$. More differentially rotating models have systematically less $J_{\rm ic,b}$ at fixed $\beta_{\rm ic,b}$ than less differentially rotating ones. This is straightforward to understand, since, at fixed $J_{\rm ic,b}$ and $M_{\rm ic,b}$, a more differentially rotating inner core will always have more rotational energy. Hence, at fixed $\beta_{\rm ic,b}$ and $M_{\rm ic,b}$, $J_{\rm ic,b}$ of a model with smaller A will be smaller.

The central rest-mass density is important for the structure and dynamics of the inner core, which turns into the unshocked protoneutron star core after bounce. In the nonrotating, low-temperature limit, the central density, for a given nuclear EOS, determines stellar structure and pulsational mode spectrum completely [83]. In Fig. 5, we plot the central density at bounce ($\rho_{\rm c,b}$ as a function of $\beta_{\rm ic,b}$; upper graphs) and the time-averaged density over the first few milliseconds after bounce ($\rho_{\rm max,pb}$ as a function of $\beta_{\rm ic,pb}$; lower graphs; we average over 6 ms, from 2 to 8 ms after bounce). Both quantities decrease with increasing total rotation, since centrifugal support keeps the core in a less compact (i.e. lower-density) configuration. The central densities of very slowly rotating models ($\beta_{\rm ic,b} \lesssim 0.02 - 0.03$) exhibit little variation with differential rotation parameter A. In more rapidly rotating models, those with smaller A (more differential rotation) have systematically slightly larger $\rho_{\rm c,b}$. Since most of their spin is concentrated at small radii (and mass coordinates), they experience less centrifugal support throughout the collapsing inner core than models with larger A at the same $\beta_{\rm ic,b}$. However, after bounce the extremely rapid rotation in the central regions of strongly differentially spinning models leads to slightly more oblate innermost cores and somewhat lower time-average postbounce densities, as shown by Fig. 5.

Figure 6 depicts 2D entropy colormaps with superposed iso-density contours at 12 ms after bounce for three representative models with $\beta_{\rm ic,b} \sim 0.1$ and differential rotation parameters $A1$ (model A1O9, strong differential rotation), $A3$ (model A3O6, moderate differential rotation), and $A5$ (model A5O5.5, nearly uniform rotation). Shown are the upper hemisphere and the rotation axis is aligned with the positive z-axis. The unshocked protoneutron star core (specific entropy $s \lesssim 3\,k_{\rm B}\,{\rm baryon}^{-1}$) is more extended in less differentially rotating models, since they have more angular momentum at larger mass (and radial) coordinates. On the other hand, the innermost regions, identified by the $10^{14.4}\,{\rm g\,cm^{-3}}$ contour line, are slightly more expanded in more differentially rotating models, in agreement with the slightly lower maximum postbounce densities shown in Fig. 5.

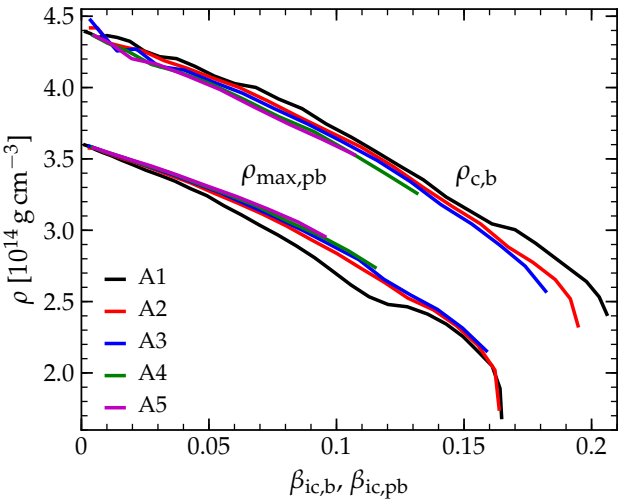

FIG. 5: The central rest-mass density at bounce $\rho_{\rm c,b}$ as a function of $\beta_{\rm ic,b}$ (upper graphs) and time-average maximum density in the postbounce phase $\rho_{\rm c,pb}$ as a function of the time-averaged $\beta_{\rm ic,pb}$ (lower graphs). We show curves for the five values of the differential rotation parameter A. Centrifugal support leads to a decrease in both the density at bounce and in postbounce core. A strong dependence on differential rotation is apparent only in very rapidly rotating models. Note that differentially rotating models develop slightly off-center density maxima and quasi-toroidal structure (cf. Fig. 6), but the maximum density exceeds the central density only by a few percent in such models.

Figure 6 also shows that overall shape of the protoneutron stars' cores varies with differential rotation. While the $A5$ model is clearly spheroidal, the density contours (traced by the entropy distribution) of the strongly differentially rotating $A1$ model show a double-lobed structure characteristic of quasitoroidal equilibrium configurations that have their maximum density not at a single point at the origin, but in a ring at some finite radius in the equatorial plane. This is expected to occur in strongly differentially rotating cores and has been reported before in, e.g., [1, 38, 40, 47]. We indeed find that the tendency to develop off-center density maxima increases with de-

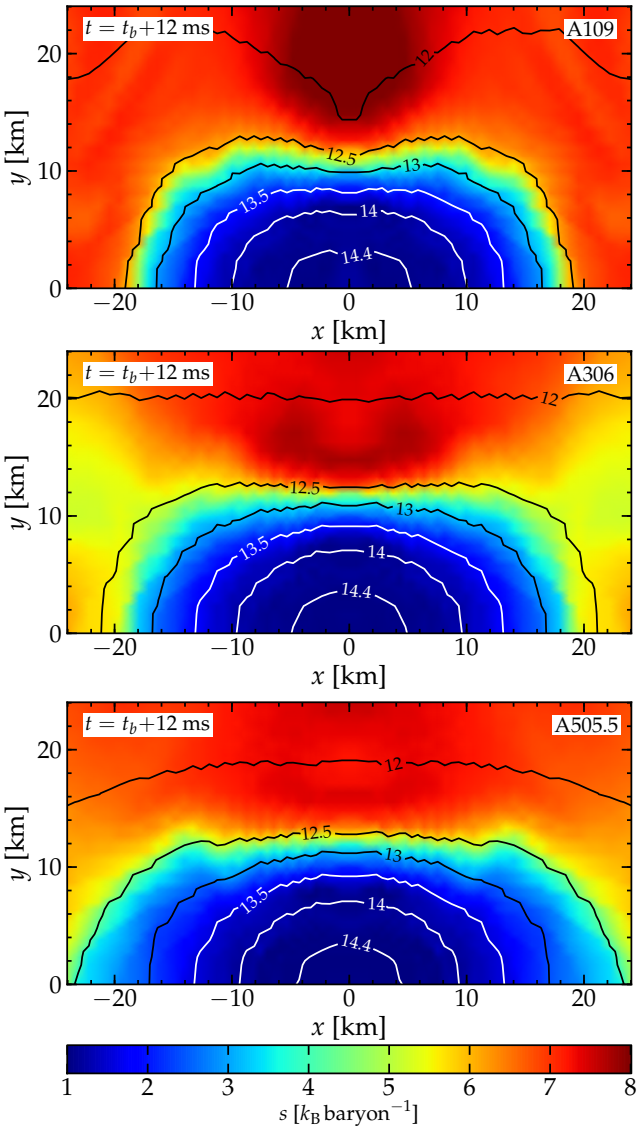

FIG. 6: Entropy colormaps of the meridional plane for models A1O9, A3O6, A5O5.5 with $\beta_{\rm ic,b} \sim 0.1$ at 12 ms after bounce. Black and white lines are mark density isocontours at 10^{12}, $10^{12.5}$, 10^{13}, $10^{13.5}$, 10^{14}, and $10^{14.4}$ g cm^{-3}. More differentially rotating models have more compact unshocked (low entropy) cores and more centrifugally deformed innermost density isocontours.

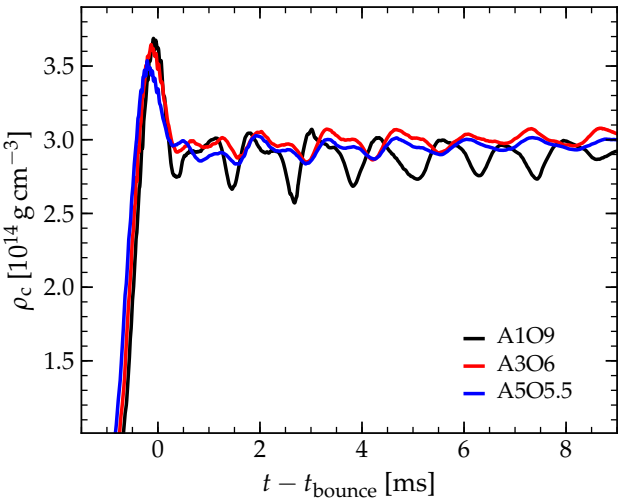

FIG. 7: Time evolution of the central density for models A1O9, A3O6, and A5O5.5, all of which have $\beta_{\rm ic,b} \sim 0.1$. More differentially rotating models more strongly overshoot their postbounce quasi-equilibrium central densities at bounce and exhibit stronger postbounce ring-down oscillations.

creasing A, but even the most rapidly differentially rotating model in our entire set has a density contrast of only $\rho_{\rm max,pb}/\rho_{\rm c,pb} - 1 \lesssim 3\%$ and its density maximum is located only $\sim$1.2 km off the origin.

In Fig. 7, we plot the evolution of the central density of the same three models (A1O9, A3O6, and A505.5) with $\beta_{\rm ic,b}$ shown in Fig. 6. At bounce, the most differentially rotating model overshoots its postbounce quasi-equlibrium the most, settles at the lowest $\rho_{\rm c,pb}$, and exhibits the strongest postbounce ringdown oscillations. These oscillations are non-linear and a superposition of multiple modes, but in previous work, at least one of the modes has been identified as the fundamental quadrupole mode of the protoneutron star core [39]. The most differentially rotating model has most of its spin concentrated in the centralmost regions. Hence, these regions are most oblate ($\ell = 2$) in this model, yielding the strongest excitation of the quadrupole core pulsation mode.

In summary and to connect to the next section on GW emission: although the important quantities $\rho_{\rm c,b}$ and $\rho_{\rm max\,or\,c,pb}$ depend primarily on $\beta_{\rm ic,b}$, we also observe a dependence on the differential rotation parameter A, in particular in rapidly rotating cases. This and the obvious differences in the 2D structure of the postbounce cores shown by Fig. 6 suggest that the detailed multi-dimensional dynamics of the GW-emitting innner core are governed not only by its total rotation, but also by the distribution of angular momentum. We shall next investigate the effect of differential rotation on the GW signal.

B. Influence of Differential Rotation on the Gravitational Wave Signal

For an analysis of the influence of the differential rotation parameter A on the GW signal, it is useful to first recap the latter's general morphology and at which point in the highly dynamical evolution of the inner core it reaches its peak values. In the following, without loss of generality, we will assume that the core's spin is aligned with the positive z-axis. The bottom panel of Fig. 2 shows the GW strain h_+ (there is only one polarization due to axisymmetry) as a function of time in the late collapse, bounce, and early postbounce phases of our reference model A3O6. During the collapse phase, h increases slowly and reaches a positive peak, $h_{1,\rm pos}$, during the rapid contraction phase immediately before bounce.

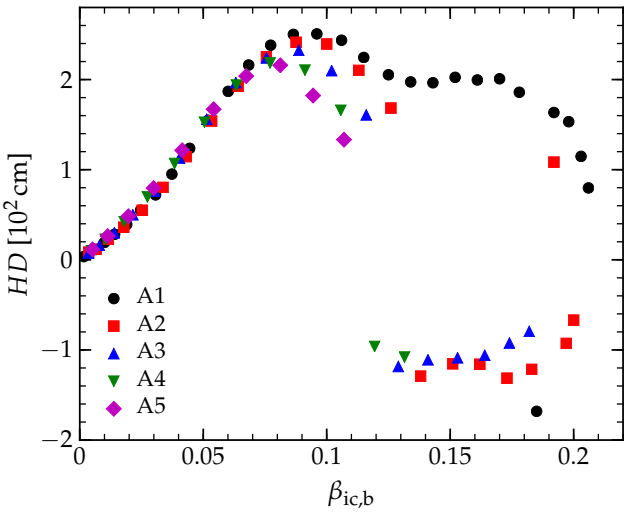

FIG. 8: Values of the second largest peak (in absolute value) H of the GW signal as a function of $\beta_{\rm ic,b}$ for all models. More differentially rotating models yield larger positive H and switch to negative H at higher $\beta_{ic,b}$. While differential rotation is a necessary criterion for $H < 0$, it is not a sufficient one.

During bounce, h decreases rapidly, reaching its most pronounced negative peak $h_{1,\rm neg}$ when the inner core is expanding at bounce (cf. the evolution of the maximum density shown in the top panel of Fig. 2). Following $h_{1,\rm neg}$, h reaches positive values and generically has a new positive local maximum, $h_{2,\rm pos}$. In slowly rotating models ($\beta_{\rm ic,b} \lesssim 0.05$), $h_{2,\rm pos}$ coincides with the first recontraction of the core after bounce. In the rapidly rotating case, an identification of $h_{2,\rm pos}$ with global core dynamics is less obvious, since bounce leads to the excitation of several oscillation modes in the core (dominated by the fundamental quadrupole mode, see [39]), which all contribute to the GW signal at this point. After $h_{2,\rm pos}$, the core undergoes ring-down oscillations that are damped hydrodynamically. They produce more peaks in h whose amplitudes decay on a timescale of $10-15$ ms. Hereafter, we refer to the peaks that occur after $h_{1,\rm neg}$ as *ring-down peaks*.

Hayama *et al.* [84] analyzed 2D Newtonian simulations of 12 models simulated by Kotake *et al.* [48] with varying rotation law and degrees of total and differential rotation. They studied the peak values of GW strain and observed that the *ring-down peak* with the *largest absolute value* – which we denote as H hereafter – is negative ($H < 0$) for models with rapid differential rotation (and a cylindrical rotation law like our Eq. 1), while for the rest of their models, H is positive and coincides with $h_{2,\rm pos}$. They argued that the detection and extraction of the *sign* of H could therefore provide clear information about the angular momentum distribution in a progenitor's iron core.

Figure 8 displays H as a function of $\beta_{\rm ic,b}$ for different values of A for all of our models. H grows almost linearly with $\beta_{\rm ic,b}$ for $\beta_{\rm ic,b} \lesssim 0.08$ for all values of A. In this regime, H is positive and corresponds to $h_{2,\rm pos}$. All values of A yield nearly identical H for a given $\beta_{\rm ic,b}$ for $\beta_{\rm ic,b} \lesssim 0.08$, implying that in this regime H is affected by the total rotation of the inner core but not by the distribution of angular momentum within the inner core.

In more rapidly rotating models ($\beta_{\rm ic,b} \gtrsim 0.08$), the values of H diverge for different A with the general trend that *more differentially rotating models yield larger positive H*. At $\beta_{\rm ic,b} \gtrsim 0.12$, H becomes negative and no longer corresponds to $h_{2,\rm pos}$. This occurs first (in $\beta_{\rm ic,b}$) for less differentially rotating models, and the most differentially rotating sequence $A1$ maintains H with only a single outlier in which a negative peak has a just slightly larger magnitude than $h_{2,\rm pos}$. From this, we conclude that the sign of H is *not a good indicator of differential rotation*. This is in disagreement with the conclusions of Hayama *et al.* [84] who drew their conclusions on the basis of a smaller set of models that explored the parameter space less systematically than our model sequences. In their defense, we note that $H < 0$ occurs only in models which have at least weak differential rotation ($A \lesssim A4$ in our model set), simply because uniformly spinning models cannot reach sufficiently high $\beta_{\rm ic,b}$ for H to become negative (Figs. 3 and 8). However, the opposite is not true; $H > 0$ does not always indicate uniform rotation.

In Fig. 9, we compare waveforms of models with the same total rotation (as measured by $\beta_{\rm ic,b}$) but different degrees of differential rotation. The top panel depicts waveforms of models with moderate rotation ($\beta_{\rm ic,b} \sim 0.05$) while the bottom panel shows waveforms of rapidly spinning models with $\beta_{\rm ic,b} \sim 0.10$. At $\beta_{\rm ic,b} \sim 0.05$, all choices of A yield essentially the same waveform between peaks $h_{1,\rm pos}$ and $h_{2,\rm pos}$ and differences appear only during the ring-down phase. The situation is different for rapidly rotating models whose dynamics are more strongly affected by rotation. While the overall shape of the bounce spike and its width are still the same for all values of A, more differentially rotating models yield larger $|h_{1,\rm neg}|$ and $h_{2,\rm pos}$. The ring-down waveform of the most differentially rotating model is very different from the other models, reflecting the much more pronounced postbounce variations in its central density (shown in Fig. 7).

The trends seen in the few select models shown in Fig. 9 in the bounce region of the waveform are very systematic. This is evident in Fig. 10, which shows the values of $h_{1,\rm pos}$, $h_{1,\rm neg}$, and $h_{2,\rm pos}$ as a function of $\beta_{\rm ic,b}$ for the five considered choices of the differential rotation parameter A. At slow rotation ($\beta_{\rm ic,b} \lesssim 0.04-0.08$) there is little dependence on differential rotation. In more rapidly rotating models, increasing differential rotation (= decreasing A) systematically decreases $h_{1,\rm pos}$, makes $h_{1,\rm neg}$ more negative, and increases $h_{2,\rm pos}$. This suggests that it should—in principle—be possible to infer the degree of differential rotation of rapidly rotating cores from the GW signal alone. In Section VI, we explore two methods that can be used to "measure" total rotation and A from an observed signal.

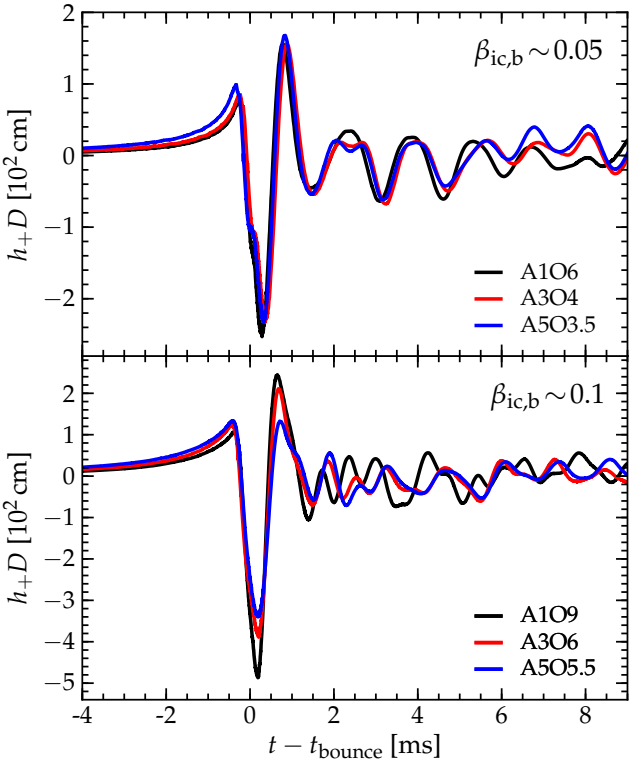

FIG. 9: GW strain h_+ rescaled by source distance D. The top panel shows three models with different degrees of differential rotation but with the same $\beta_{\rm ic,b} \sim 0.05$. The bottom panel shows three more rapidly spinning models with $\beta_{\rm ic,b} \sim 0.1$. In the first case, the three models exhibit almost identical GW signals from bounce, suggesting little sensitivity to differential rotation. The situation is different in the rapidly rotation case, where there is significant variation between models with different values of the differential rotation parameter A.

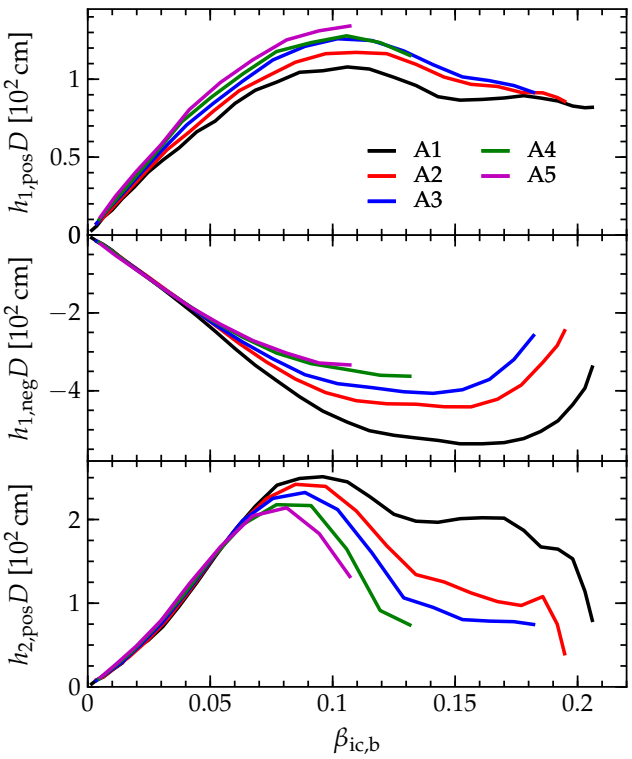

FIG. 10: The values of the first three peaks of the GW strain $h_{1,\rm pos}$, $h_{1,\rm neg}$, $h_{2,\rm pos}$ (cf. Fig. 2) as a function of $\beta_{\rm ic,b}$ plotted for all five model sequences. These three prominent GW signal peaks are insensitive to the angular momentum distribution for slowly rotating models that reach $\beta_{\rm ic,b} \lesssim 0.05 - 0.08$. More rapidly rotating models show clear trends with differential rotation.

VI. RESULTS: EXTRACTING THE ANGULAR MOMENTUM DISTRIBUTION FROM AN OBSERVED SIGNAL

A. Numerical Template Bank Analysis

As our analysis in the previous section suggests, the peak strain amplitude of the GW signal from rotating CCSNe is dependent on the differential rotation parameter A. However, much more information than this (*e.g.*, power spectrum) is encoded in the GW waveforms. To assess the dependence of all signal features on $\beta_{\rm ic,b}$ and A and the detectability of these signatures, we employ a *matched filter* technique. In the case of a known signal in Gaussian noise, it is well known that the *matched filter* is the optimal technique for detection [85]. This method cross-correlates the GW data observed with a series of 'template' waveforms, produced from the GW emission model for the source. The GW signal from rotating collapse, bounce, and ring-down oscillations can be modeled deterministically to a high precision for a given EOS and neutrino microphysical model, suggesting that the matched filter approach should be optimal in this context.

In this vein, we pursue the construction of a numerical template bank analysis for the GW signals from all models described in Tables I–II. We then inject a new set of waveforms into simulated Gaussian detector noise to determine the template that best fits the data. To produce these waveforms, we perform a new set of simulations for all values of A and for a broad range of rotation rates from slow to very rapid. In these models, the values of $\Omega_{\rm c}$ are chosen to differ by 0.25 rad/s from those included in the template bank. As mentioned earlier, the latter models differ in $\Omega_{\rm c}$ by 0.5 rad/s from their "neighboring" models. Therefore, for each injected model, there are two models from the PC catalog that have central angular velocities larger and smaller by 0.25 rad/s than that of the injected model. As $\beta_{\rm ic,b}$ and A are known for all template waveforms, the determination of the maximum likelihood template for a given injected signal will suggest its associated $\beta_{\rm ic,b}$ and A.

We model the GW detector data, $\tilde{d}$, assumed to be comprised of both some CCSN signal, $\tilde{h}(f;\vec{\theta})$, and Gaussian noise $\tilde{n}$ colored by known one-sided power spectral

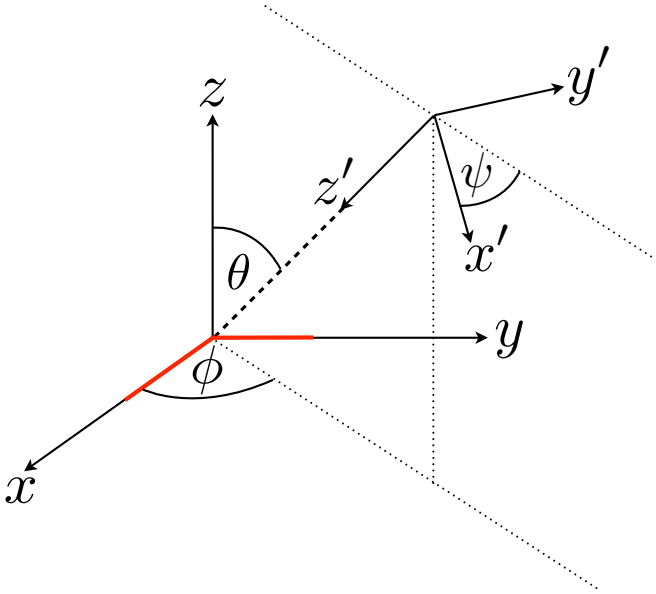

FIG. 11: The angles (θ, ϕ, ψ) between a GW detector (located at the origin of the unprimed frame and aligned in the $x-y$ plane) and GW propagating in the z' direction.

density (PSD) $S_h(f)$, as

$$\tilde{d}_i = \tilde{h}(f_i; \vec{\theta}) + \tilde{n}_i, \tag{2}$$

where i denotes the frequency bin index. We perform the following analysis in the Fourier domain due to frequency dependence and Gaussian statistics of $\tilde{n}$.

The parameter dependence of the GW signals considered here is encoded in $\vec{\theta}$, where

$$\vec{\theta} = \{\vec{\epsilon}, d, t_0, \alpha, \delta, \theta, \phi, \psi\}, \tag{3}$$

where d is the source distance, t_0 is the GW arrival time and $(\alpha, \delta, \theta, \phi, \psi)$ are source angles. Here, (α, δ) are the right ascension and declination of the source, while (θ, ϕ, ψ) define the relationship between the sky GW detector frames, as shown in Figure 11.

Our goal is to compute the likelihood $\mathcal{L}^j$ for each template $\tilde{x}^j$, given $\tilde{d}_i$, where ^{j} denotes the template index. Assuming stationary, Gaussian detector noise, the likelihood of a particular template can be calculated as

$$\mathcal{L}^j \propto \prod_i \exp\left(-2\Delta f \frac{|\tilde{d}_i - \tilde{x}_i^j|^2}{S_h(f_i)}\right), \tag{4}$$

where $\Delta f = 1/T$ is the frequency resolution of the Fourier domain data.

It is then possible to consider the set of likelihoods $\mathcal{L}^j$, and determine which of the templates best fits the observed data. We compute the relative log likelihood between templates i and j respectively as $\log \mathcal{L}^{i;j} = \log \mathcal{L}^i - \log \mathcal{L}^j$, to determine whether it is more likely that the observed data contains a signal of the form of template i ($\log \mathcal{L}^{i;j} > 0$) or of the form of template j ($\log \mathcal{L}^{i;j} < 0$). We impose a threshold ξ, such that any instance of $\log \mathcal{L}^{i;j} > \xi$ is statistically significant, and asserts that the injected signal is more likely to be of the form of template i than template j. For the purposes of this work, we require that $\mathcal{L}^{\max;j} > 5$, where $\mathcal{L}^{\max}$ is the maximum likelihood produced, and j encompasses all other templates.

We use simulated Gaussian noise colored by the zero-detuned high power configuration of aLIGO [2], in the context of a single, optimally-oriented GW detector. We assume that the angles $(\alpha, \delta, \theta, \phi, \psi)$ are known, and are such that the antenna response functions, F_+ and $F_\times$, where

$$F_+ = \frac{1}{2}(1 + \cos^2\theta)\cos 2\phi \cos 2\psi - \cos\theta \sin 2\phi \sin 2\psi, \tag{5}$$

$$F_\times = \frac{1}{2}(1 + \cos^2\theta)\cos 2\phi \sin 2\psi + \cos\theta \sin 2\phi \cos 2\psi, \tag{6}$$

are equal to 1 and 0 respectively. In physical terms, this corresponds to a source where $(\theta, \phi, \psi) = (0, 0, 0)$. We place all sources at a known distance of 10 kpc, restricting our analysis to the galactic locus.

1. *Extraction of* $\beta_{\rm ic,b}$

The upper panel of Fig. 12 shows $\beta_{\rm ic,b}$ measured for injected waveforms versus the true values of $\beta_{\rm ic,b}$ of those models. The dashed black line denotes the optimal case in which the measured and true $\beta_{\rm ic,b}$ are identical. For all injected waveforms, the value of $\beta_{\rm ic,b}$ measured lies within $\sim 10\,\%$ of the true value for all injected waveforms spanning the five models of A considered, with $\beta_{\rm ic,b}$ ranging from ~ 0.01 to ~ 0.2. The average relative deviation of measured $\beta_{\rm ic,b}$ from its true value is $\sim 7\,\%$ for all injected waveforms. This suggests that the matched filter analysis can extract $\beta_{\rm ic,b}$ with fair accuracy across a wide range of both total and differential rotation parameters. This is not surprising, as we demonstrated in the previous section that the GW signal amplitudes depend primarily on $\beta_{\rm ic,b}$ both for slowly and rapidly rotating models. It can be therefore be deduced that the waveforms considered contain clear and easily extractable information about $\beta_{\rm ic,b}$.

In order to test the robustness of this conclusion, we explore the accuracy with which this analysis can extract $\beta_{\rm ic,b}$ for injected signals that are produced using a different nuclear EOS or different $Y_{\rm e}(\rho)$ parametrization. Differences in these two are associated with differences in the pressure, energy density, and other thermodynamic quantities, which can lead to differences in the dynamics of core collapse, bounce, and ring-down oscillations. The EOS dependence in the context of GW emision from rotating stellar core collapse, bounce, and ring-down oscillations was explored by [38], while the influence of $Y_{\rm e}$ parametrization was studied by [40].

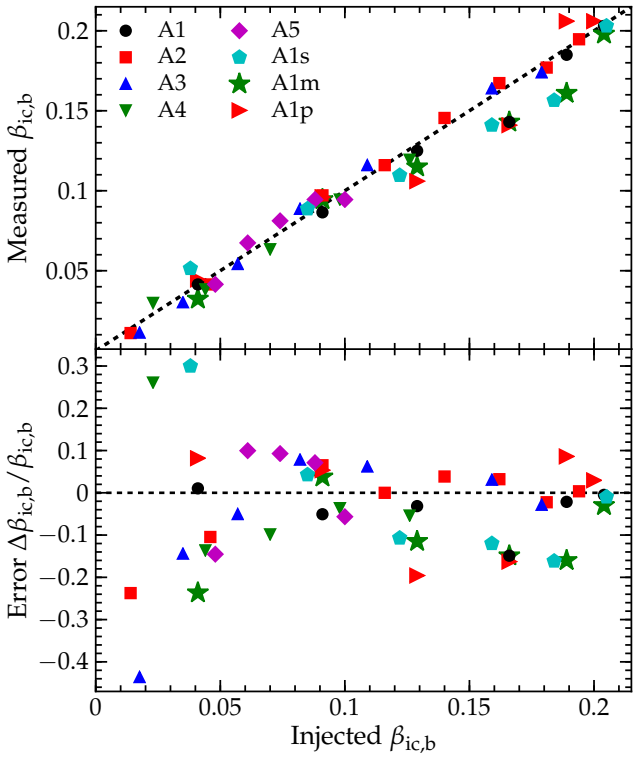

FIG. 12: Upper panel: Measured $\beta_{\rm ic,b}$ as a function of true $\beta_{\rm ic,b}$ for all injected waveforms. The dashed black line denotes the optimal optimal case in which the measured and true $\beta_{\rm ic,b}$ are identical. For all models, it can be seen that $\beta_{\rm ic,b}$ is measured with $\sim 10\,\%$ accuracy. Lower panel: the relative deviation of the measured $\beta_{\rm ic,b}$ from its true value.

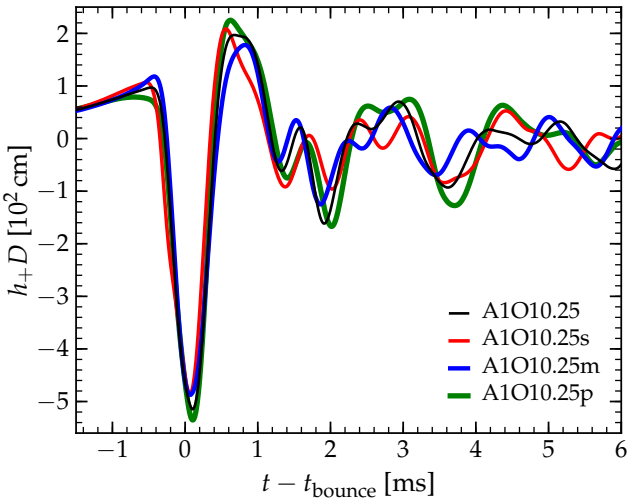

FIG. 13: GW strain h_+ rescaled by source distance D for injected waveforms A1O10.25. The black line represents the waveform generated using the Lattimer-Swesty EOS [60] and the standard $Y_{\rm e}(\rho)$ parametrization, the red line corresponds to the model simulated with the Shen *et al.* [58, 65] EOS, while the blue and magenta lines are simulated with $\sim 5\,\%$ increased and decreased $Y_{\rm e}(\rho)$ at nuclear densities.

In order to test the EOS dependence, we repeat the model sequence $A1$ for injection with the Shen *et al.* [58, 65] EOS instead of the Lattimer & Swesty EOS [60] used in the fiducial models listed in Tables I-II. For these simulations, we use the same $Y_{\rm e}(\rho)$ parametrization as for our fiducial models. We hereafter refer to this sequence as A1s. To explore the dependence of the GW signals on the $Y_{\rm e}$ parametrization, we repeat the same sequence with the Lattimer & Swesty EOS but with $\sim 5\,\%$ increased and decreased $Y_{\rm e}$ at nuclear density (sequences A1p and A1m, respectively). The details of this parametrization are explained in Appendex A, while the details of the models from these sequences are given in Table III.

Fig. 13 shows the GW strain versus time for models A1O10.25 from the injected sequences A1, A1m, A1p, and A1s during the late collapse, bounce, and early post-bounce phases. Although the behavior of the GW strain appears qualitatively similar in these four cases, there are non-negligible quantitative differences stemming from the changes in the EOS and $Y_e(\rho)$ parametrization. In the following, we explore how this affects the extraction of $\beta_{\rm ic,b}$ by filtering signals from sequences A1s, A1m, and A1p through our template bank.

The cyan pentagons in Fig. 12 display the measured $\beta_{\rm ic,b}$ as a function of the true $\beta_{\rm ic,b}$ for sequence A1s. Despite the difference between the two EOSs, the matched filtering analysis measures $\beta_{\rm ic,b}$ within $\lesssim 15\,\%$ of its correct value for all waveforms considered. The average relative deviation between measured and true $\beta_{\rm ic,b}$ for all A1s models is $\sim 10\,\%$. Such small deviations are not surprising given the somewhat weak dependence of the GW features from rotating collapse, bounce, and ring-down on the details of the EOS [38]. The green stars and red triangles in Fig. 12 represent the measured $\beta_{\rm ic,b}$ as a function of true $\beta_{\rm ic,b}$ for sequences A1m and A1p, respectively. Here we see again that $\beta_{\rm ic,b}$ is extracted with $\lesssim 15\,\%$ accuracy with an average deviation of $\sim 10\,\%$ for the entire injected model set.

Based on these results, we conclude that our matched filter analysis can extract $\beta_{\rm ic,b}$ robustly with $\sim 10\,\%$ accuracy for GW signals from rotating collapse, bounce, and ring-down oscillations from Galactic CCSNe.

2. *Extraction of A*

The upper panel of Fig. 14 shows the quantity $\delta i = {\rm IDX}[A_{\rm meas.}] - {\rm IDX}[A_{\rm inj.}]$ as a function of $\beta_{\rm ic,b}$, where ${\rm IDX}[A_{\rm meas.}]$ is the index of the differential rotation parameter $A_{\rm meas.}$ extracted by the matched filter analysis, while Idx.$[A_{\rm inj.}]$ is the index of the true value of A for the injected signal (e.g., Idx.$[A] = 2$ for $A = A2$). In this construction, $\delta i = 0$ ($\delta i \neq 0$) for the correct (incorrect) measurement of A.

For the uniformly rotating model $A5$, A is identified correctly for all injected signals. For sequences $A4$ ($A3$), A is determined accurately for 60% (66%) of injected

waveforms, while all injections except one are identified correctly for the $A2$ and $A1$ sequences. Moreover, A was found to correspond to the next closest value in the majority of misidentification cases. At $\beta_{\rm ic,b} \gtrsim 0.12$, A is correctly determined for all injected waveforms. This asserts our previously introduced notion that angular momentum distribution plays a more significant role only at rapid rotation.

For sequence A1s, A is measured correctly only for the most rapidly rotating model, where $\beta_{\rm ic,b} \sim 0.2$ (shown with cyan pentagons in Fig. 14 and denoted as A1s).

This suggests that, unlike for $\beta_{\rm ic,b}$, the inference of A is highly sensitive to details of the nuclear EOS. This is due to the instrinsically weaker dependence of the GW emission on A in comparison to $\beta_{\rm ic,b}$. This means that features signifying A can be confused with features imprinted due to differences in the EOS. Confirming this conclusion, A is extracted correctly only in the case of rapid rotation, as such models reach lower densities than do those with slow rotation, where the two nuclear EOSs differ less than in the high density regime.

For the A1m and A1p models, A is inferred correctly for 67% and 83% of injections, respectively.

To further assess the robustness of these findings, we consider the waveform injections characterised by A not encompassed by the template bank. Here, we aim to assess whether or not our analysis can determine the closest value of A in the template bank to that of the injected signal, when the correct A is not available. The lower panel of Fig. 14 presents δi as a function of $\beta_{\rm ic,b}$ for this scenario. Here, $\delta i = \pm 1$ implies $A_{\rm meas.}$ is estimated to be the closest available value of A. For $A4$ and $A5$, all injections are associated with the closest Ai. For $A3$, just under half the injections are found with $\delta i = \pm 1$, while the remainder have $\delta i = 2$. For sequence $A2$, constrastingly, all injections except the most slowly rotating return the optimal result of $\delta i = \pm 1$. For sequence $A1$, 67% of injections return $\delta i = \pm 1$, while the remainder return $\delta i = 2, 3$. Further confirming previous results, we find that injections from the A1s, A1m, and A1p models have significantly larger values of $|\delta i|$ than A1.

Summarising, in the case of 'known' EOS and $Y_{\rm e}(\rho)$ parametrization, the matched filter measures A with average $|\delta i|$ of 0.218. If the EOS and $Y_{\rm e}(\rho)$ are 'unknown', then this number increases to 0.714. If the value of A of the injected signal is not available in the template bank catalog, then these two numbers increase to 1.094 and 1.476, respectively.

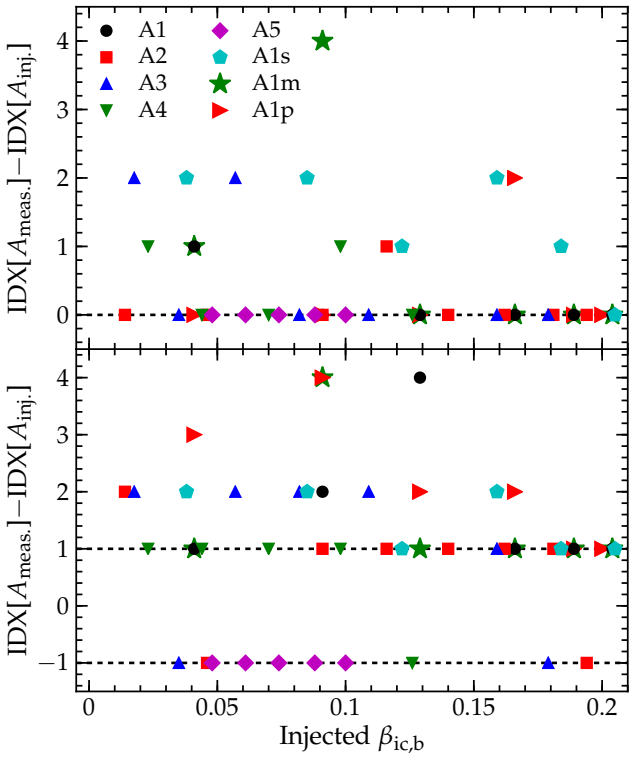

FIG. 14: The quantity $\delta i = {\rm IDX}[A_{\rm meas.}] - {\rm IDX}[A_{\rm inj.}]$ as a function of $\beta_{\rm ic,b}$, where IDX$[A_{\rm meas.}]$ denotes the index of differential rotation parameter $A_{\rm meas.}$ extracted using the matched filter analysis, and Idx.$[A_{\rm inj.}]$ is the index of the true value of A for the injected signal (e.g., Idx.$[A] = 2$ for $A = A2$). As mentioned previously, $\delta i = 0$ ($\delta i \neq 0$) represent the cases in which A is correctly (incorrectly) identified. The upper and lower panels represent the cases in which the true value of A is and isn't emcompassed by the template bank, respectively.

B. Bayesian Model Selection

To further assess the dependence of the features of the GW signal on the differential rotation parameter A and its detectability, we employ a Bayesian analysis utilising principal component analysis (PCA) [86], building upon previous research by Röver *et al.* [87] and Logue *et al.* [66].

As discussed in previous sections, GW signals from progenitors characterized by any given A are expected to exhibit some strong common features. To exploit this, we apply PCA to catalogs of waveforms characterised by a common A for each value of A. PCA isolates dominant features of waveforms into linearly independent principal components (PCs), ordered by their relevance. Mathematically, utilizing matrix C containing a given waveform catalog, one can factorize C as

$$C = U \Sigma V^T, \tag{7}$$

where U and V are matrices comprised of the eigenvectors of CC^T and C^TC respectively, and Σ is a diagonal matrix, composed from the square roots of corresponding eigenvalues. The PCs, U, are organized according to their corresponding eigenvalues, such that the more dominant PCs (characterized by larger eigenvalues) are shifted to the first few columns of U. Approximations to waveforms in C, in addition to arbitrary waveforms, can be constructed as

$$h_i \approx \sum_j U_{ij} \epsilon_j, \tag{8}$$

where h is the desired waveform approximation, and $\vec{\epsilon}$ contains the projections of the original waveforms onto the U basis, hereafter referred to as PC coefficients.

As in the previous section, we model the GW detector data, $\tilde{d}$, as containing both the CCSN signal $\tilde{h}(f;\vec{\theta})$ and Gaussian noise $\tilde{n}$, colored by a known one-sided power spectral density (PSD) $S_h(f)$, where $\tilde{d}$ and $\vec{\theta}$ are given by expressions (2) and (3) respectively.

Our goal is to compute the evidence, $p(d|\mathcal{H})$, that the data observed contains a GW signal reconstructable from different sets of PCs, each associated with a particular degree of differential rotation. The evidence, or marginal likelihood, of the model $\mathcal{H}$ is calculated as

$$p(d|\mathcal{H}) = \int_{\vec{\theta}} p(d|\vec{\theta};\mathcal{H}) p(\vec{\theta}|\mathcal{H})\, d\vec{\theta}, \tag{9}$$

where $p(\vec{\theta}|\mathcal{H})$ is the prior distribution on the parameters, given the signal model (assumed to be log-flat in the absence of any physical motivation to do otherwise) and $p(d|\vec{\theta};\mathcal{H})$ is the likelihood function for the data. Due to the Gaussian statistics of the noise, the likelihood function for the presence of some signal $\tilde{h}(f_i;\vec{\theta})$ can be written as

$$p(d|\vec{\epsilon};\mathcal{H}) = \prod_i \frac{1}{\sigma_i\sqrt{2\pi}} \exp\left(-\frac{|\tilde{d}_i - \tilde{h}(f_i;\vec{\theta})|^2}{2\sigma_i^2}\right). \tag{10}$$

Here, σ_i^2 is the variance of the noise in the i^{th} frequency bin, related to the PSD as

$$S_h(f_i) = 2\frac{\Delta t^2}{T}\sigma_i^2, \tag{11}$$

where Δt and T are the sampling time-step (the inverse of the sampling frequency) and the total observation time, respectively. To compute the evidence, we utilise an implementation of the nested sampling algorithm [88].

We perform an analysis closely linked to previous work by [66, 87]. As previously mentioned, it is desirable to construct PC sets from waveform catalogs assembled from progenitors with distinct, discrete values of A, as these bases contain dominant features characteristic of their associated values of A. In defining five models, each describing GW signals with differential rotation of $A1,\ldots,A5$, with which to analyze GW signals of arbitrary A, we can demonstrate the ability of each basis to represent the distinguishing features of an observed signal.

We compute the relative Bayes factor, $\log B_{i;j} = \log p(d|i) - \log p(d|j)$, between models i and j, to determine whether the evidence for model i is either greater than ($B_{i;j} > 0$) or less than ($B_{i;j} < 0$) the evidence for model j.

Connecting this to the physical motivation of our analysis, models i and j denote PC sets constructed from waveforms characterized by different degrees of differential rotation. Further to this, we 'normalize' the Bayes factor for the correct differential rotation PC set B_{true} for each injected signal, to present the degree to which the correct PC set is either preferred or rejected, relative to the other PC sets B_j. To do this, we compute

$$\log B_{\text{true};j} = \log B_{\text{true}} - \log B_j \geq 0, \tag{12}$$

if $\log B_{\text{true}} \geq \log B_j$, for all j. If, however, $\log B_{\text{true}} < \log B_j$ for some j, we compute

$$\log B_{\text{true};j} = \log B_{\text{true}} - \max[\log B_j] < 0. \tag{13}$$

In doing this, the statement $\log B_{\text{true};j} > 0$ affirms that the most likely degree of differential rotation chosen is that of the injected signal, while $\log B_{\text{true};j} < 0$ asserts the opposite outcome. We impose a threshold η, such that any instance of $\log B_{i;j} > \eta$ is statistically significant, and asserts that the injected signal is more likely characterized by the degree of differential rotation, Ai, rather than Aj. In this paper, we designate $\eta = 5$.

As in the previous section, for the purposes of this work, we utilize simulated Gaussian noise colored by the zero-detuned high power configuration of aLIGO [2], in the context of a single, optimally-oriented GW detector. We assume that the position, inclination, and polarization of the source are known, such that the antenna response functions are given by $F_+ = 1$, $F_\times = 0$. We place all sources at a known distance of 10 kpc. We use a subset of 10 PCs from each set to reconstruct the injected waveforms, a quantity chosen due to limitation by the smallest number of waveforms in one waveform catalog. Given this, the parameter space $\vec{\theta}$ is reduced to a 10-dimensional subset, such that $\vec{\theta} \to \vec{\epsilon}$, where $\vec{\epsilon} = \{\epsilon_1,\ldots,\epsilon_{10}\}$.

We construct PCs using the model waveforms described in Tables I and II. To ensure the robustness of our method, we inject signals not included in the aforementioned waveform catalogs, such that no advance knowledge about observed signals is inherently assumed. In order to make quantitative statements on the efficacy of this analysis relative to the aforementioned template bank approach, we inject the same waveforms used for the matched filter analysis in the previous section.

We briefly note here that due to the nature of the PC construction method, we are unable to infer $\beta_{\text{ic,b}}$ for injected signals using the Nested Sampling analysis, unlike for the previously explored Matched Filter method. This is due to the requirement for a *catalog of waveforms*, each characterised by the same value of $\beta_{\text{ic,b}}$ to construct a model PC set. In the context of the work in this paper, we consider five models for the differential rotation parameter A, limiting the maximum number of PCs for any $\beta_{\text{ic,b}}$ model used for waveform reconstruction to five, in comparison to the 10 PCs utilised for each A model. Further to this, the range of $\beta_{\text{ic,b}}$ considered for any given A is limited, as previously mentioned, to the point at which the progenitor is completely centrifugally supported at the start of the simulation. This means that models describing a smaller degree of differential rotation cannot support highly rapidly rotating progenitors, further reducing the size of the waveform catalog at larger

$\beta_{\rm ic,b}$. Due to this, we cannot at present construct PC sets describing different models for $\beta_{\rm ic,b}$ comparable to those for A, and as such, delay this analysis to a time in the future.

Figure 15 presents the normalized $\log B_{i,j}$ for all injected waveforms.

As explained previously, the results $\log B_{i,j} > 0$ and $\log B_{i,j} < 0$ convey that, given the injected signal, the evidence is highest for the correct and incorrect model for A, respectively. It should additionally be noted that large values of $\log B_{i,j}$ indicate a high degree of confidence that the correct model for A has been chosen. The dashed black line represents the detectability threshold $\log B_{i,j} = \eta$ discussed above. At $\beta_{\rm ic,b} \lesssim 0.05$, most injected signals across all A have negative $\log B_{i,j}$, suggesting that it is difficult to infer the correct model for A at low rotation. This is consistent with our analysis of the GW peaks (Section V B), where we find almost no influence of A in the very low rotation limit of $\beta_{\rm ic,b}$. At a given $\beta_{\rm ic,b}$, model $A1$, which is the most strongly differentially rotating, has the largest $\log B_{i,j}$, suggesting that the ability to infer A with this method is greatest in extremely differentially rotating models. We also see that the magnitude of $\log B_{i,j}$ tends to grow with increasing $\beta_{\rm ic,b}$, and the correct model for A is determined for $\beta_{\rm ic,b} \gtrsim 0.08$. This is consistent with our analysis of GW peaks, where we observed significant dependence on A in the regime where $\beta_{\rm ic,b}$ is large. This indicates that, with this method, the accurate extraction of the correct model for A is possible only in rapidly rotating models with $\beta_{\rm ic,b}$ above ~ 0.08.

In order to test the robustness of this conclusion, we inject the waveform set A1s simulated with the Shen *et al.* EOS [58, 65], described in the previous section. We find that in this case, the correct model for A is determined only in the case of very rapid rotation ($\beta_{\rm ic,b} \gtrsim 0.16$). The maximum densities reached in these cases are relatively low, and as such, the two EOSs to do not differ significantly. In the low rotation limit, the injected signals are strongly associated with different models for A. This constrasts strongly with results for $A1$, where the EOS is 'known', where the correct model for A is consistently inferred strongly. This suggests that, if the differences between the true nuclear EOS and that used for PC construction are of the same order as the differences between the Lattimer & Swesty [60] and Shen *et al.* [58, 65] EOSs, then the inference of the progenitor's angular momentum distribution from the GW signal observed is significantly more difficult than if the nuclear EOS were known. This conclusion is consistent with that of the template bank analysis presented in the previous section.

Further to this, we inject waveform sets A1m and A1p, simulated with modified $Y_{\rm e}(\rho)$ parametrization, as explained in the previous section. For these injections (marked with large green stars and red triangles, respectively, in Fig. 15), it can be seen that the correct model for A is determined in the limit of high rotation, whereas the wrong model is chosen in the low rotation regime. In addition, it can be seen that for models with correctly chosen A, the magnitude of $\log B_{i,j}$ is significantly smaller than for injections from the $A1$ model, where the $Y_{\rm e}(\rho)$ parametrization is 'known'. This suggests that if the $Y_{\rm e}(\rho)$ parametrization used to generate the waveform catalogs utilized to construct the PCs does not treat the deleptonization and other neutrino effects during collapse with sufficient accuracy, the inference of the correct model for A suffers significantly.

The upper panel of Fig. 16 shows $\delta i = {\rm IDX}[A_{\rm meas.}] - {\rm IDX}[A_{\rm inj.}]$ (as previously defined) as a function of $\beta_{\rm ic,b}$ for the injected waveforms. Here, ${\rm IDX}[A_{\rm meas.}]$ is the index of the differential rotation parameter $A_{\rm meas.}$ determined by the Model Selection analysis, where $\log B_{\rm meas,j} > 5$ by definition.

It can be seen that for most injections, $\delta i = 0$, signifying that the correct model for A has been inferred. We note that the fraction of injections with $\delta i = 0$ grows with increasing $\beta_{\rm ic,b}$, which is consistent with the previous conclusion that the ability to determine A with accuracy is greater for rapidly rotating models. Further to this, it can be seen that the average value for $|\delta i|$ is much larger for waveform sequences A1s, A1m, and A1p, which is again consistent with the template bank analysis. The lower panel of Fig. 16 shows δi as a function of $\beta_{\rm ic,b}$ for the case of injections with 'unknown' A. In this case, we see that the majority of injected models have $\delta i = \pm 1$, implying identification with the closest A to that injected. Measurement of A once more improves with incresing $\beta_{\rm ic,b}$.

Summarising, in the case of 'known' EOS and $Y_{\rm e}(\rho)$ parametrization, this method extracts A with average $|\delta i|$ of 0.311. If the EOS and $Y_{\rm e}(\rho)$ are 'unknown', then this number increases to 0.571. If the value of A of the injected signal is not available in the PC catalog, then these two numbers increase to 1.136 and 1.381, respectively.

Overall, it can be seen that results obtained using both the template bank and nested sampling analyses are in qualitative agreement. Moreover, the four average values of $|\delta i|$ quoted above agree with the corresponding numbers from the matched filter method mentioned at the end of Section VI A with $\lesssim 20\%$ accuracy. This suggests that the results of these two methods are also in close quantitative agreement.

VII. SUMMARY AND CONCLUSIONS

Observations of stellar surface velocities show that most massive stars rotate and some do so with velocities close to break-up (e.g., [89, 90]). The internal distribution of angular momentum is, however, rather uncertain, and this is true in particular for the cores of presupernova stars. Rotation can influence the collapse, bounce, and postbounce dynamics and may play a role in driving the explosion. It is thus important to understand - or better, measure - the angular momentum distribution in

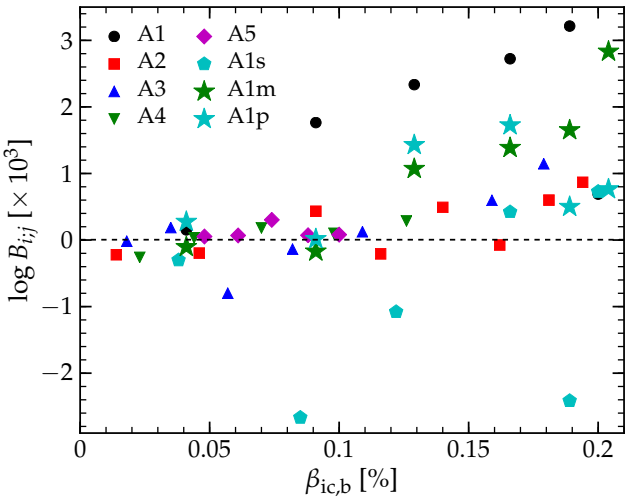

FIG. 15: $\log B_{i,j}$ for all injected waveforms. Values of $\log B_{i,j} > 0$ and $\log B_{i,j} < 0$ imply correct and incorrect inference of A, respectively. Large values of $\log B_{i,j}$ convey that the correct model has been chosen with a high degree of confidence. The black dashed line represents the detectability threshold $\log B_{i,j} = 5$ (see main text for the definition of this threshold). We see that $\log B_{i,j}$ increases with $\beta_{\rm ic,b}$, and at a given $\beta_{\rm ic,b}$, A is inferred correctly with the highest confidence for injections associated with the strongest differential rotation ($A1$). We note that in the limit of low rotation ($\beta_{\rm ic,b} \lesssim 0.05$), the correct model for A is not determined for most injections. Further to this, incorrect A is chosen for all injections simulated with the Shen *et al.* [58, 65] EOS (A1s), the incorrect model for A is chosen for all injections, with the exception of a single model characterised by extremely rapid rotation ($\beta_{\rm ic,b} \sim 0.16$.

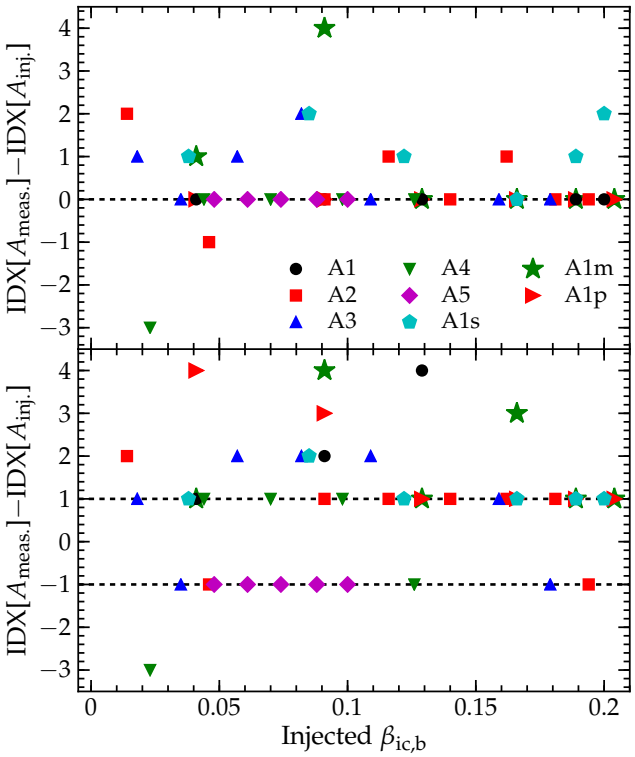

FIG. 16: The quantity $\delta i = {\rm Idx.}[A_{\rm meas.}] - {\rm Idx.}[A]$ as a function of $\beta_{\rm ic,b}$, where ${\rm Idx.}[A_{\rm meas.}]$ is the index of the differential rotation parameter $A_{\rm meas.}$ inferred by the Nested Sampling analysis, and ${\rm Idx.}[A]$ is the index of the true value of A (e.g., ${\rm Idx.}[A] = 2$ for $A = A2$). The upper and lower panels display results for cases in which A for all injections is known and unknown, respectively.

the cores of massive stars. As we have shown in this paper, the observation of gravitational waves from the next galactic core-collapse supernova may offer us the opportunity to do just that.

We have carried out an extensive set of axisymmetric general-relativistic simulations of rotating core collapse to study the influence of the angular momentum distribution on the gravitational wave signal of rotating collapse, bounce, and the very early postbounce ring-down phase. In total, we have simulated 124 different models, systematically probing the effects of "total rotation" (parameterized either by the angular momentum of the homologous inner core at bounce or by $\beta_{\rm ic,b} = T/|W|\big|_{\rm ic,b}$) and the precollapse degree of differential rotation. We have also performed simulations with a different nuclear equation of state (EOS), variations in the electron fraction of the inner core, and increased numerical resolution to test for systematic uncertainties. We have employed a single presupernova stellar model, since [39] have shown that for a given angular momentum distribution as a function of enclosed mass, EOS, and electron-capture treatment, the universal nature of core collapse [91, 92] washes out variations due to differences in precollapse progenitor structure.

Our results show that the global dynamics of rotating core collapse is almost insensitive to the precise distribution of angular momentum within the inner core. We find that there is a simple linear mapping between the two total rotation measures $J_{\rm ic,b}$ and $\beta_{\rm ic,b}$ and the centrifugally-enhanced mass of the inner core at bounce, $M_{\rm ic,b}$ throughout most of the explored parameter space. Variations in the angular momentum distribution become relevant to the overall dynamics of collapse and bounce only in very rapidly rotating cases with $\beta_{\rm ic,b} \gtrsim 0.13 - 0.15$, which corresponds to an inner-core angular momentum at bounce of $J_{\rm ic,b} \gtrsim 5 - 6 \times 10^{48}\,{\rm erg \cdot s}$ and early postbounce density-weighted average core spin periods of $\lesssim 8 - 10\,{\rm ms}$. However, differential rotation does significantly affect the structure and postbounce evolution of the protoneutron star even in more slowly spinning cores. At fixed total rotation at bounce, more differentially rotating inner cores have more centrifugally-deformed (oblate) innermost regions while their overall shape is less oblate than that of their more uniformly spinning counterparts that have more centrifugal support at greater radii (and enclosed-mass coordinates).

In slowly rotating models ($\beta_{\rm ic,b} \lesssim 0.05$), however, the degree of precollapse differential rotation has little influ-

ence on the GW signal and there are simple linear relationships that allow one to map back from the amplitude of the pronounced bounce peak $h_{1,\rm neg}$ to $J_{\rm ic,b}$ and $\beta_{\rm ic,b}$: $J_{\rm ic,b} \approx 2.2 \times 10^{48}\,{\rm erg \cdot s}$ and $\beta_{\rm ic,b} \approx 0.05$.

The structural changes due to differential rotation have important ramifications for the GW signal in more rapidly spinning models with $\beta_{\rm ic,b} \gtrsim 0.05 - 0.08$ ($J_{\rm ic,b} \gtrsim 2 - 3 \times 10^{48}\,{\rm erg \cdot s}$), corresponding to early-postbounce protoneutron star spin periods of $\lesssim 12-16\,{\rm ms}$. More differentially rotating models yield higher global peak GW strain amplitudes at bounce and emit more energy in GWs. Total rotation *and* the degree of differential rotation influence the values of the first three local extrema of the GW signal, $h_{1,\rm pos}$, $h_{1,\rm neg}$, $h_{2,\rm pos}$, in a highly systematic way.

We have exploited this systematic dependence. Our results show that it is possible to extract both total rotation (both $\beta_{\rm ic,b}$ and $J_{\rm ic,b}$, since the two are simply related) and the degree of differential rotation from a previously *unknown* observed galactic ($D = 10\,{\rm kpc}$) rotating core collapse GW signal via simple cross-correlation with waveforms from a numerical template GW signal bank created from our model GW signals. Since more rapidly spinning cores produce stronger signals, this works best for rapid rotation and our matched-filtering template-bank method can *measure* total rotation to within $\sim 15\%$ for a rapidly rotating ($\beta_{\rm ic,b} \gtrsim 0.08$) core at $D = 10\,{\rm kpc}$ that is optimally oriented with respect to a single GW detector. Measuring total rotation is also possible for more slowly spinning cores, though the errors, even for an optimally oriented core, may be $\lesssim 45\%$. For rapidly rotating cores ($\beta_{\rm ic,b} \gtrsim 0.08$) the differential rotation parameter A of the employed rotation law can be extracted with good precision (maximum offset of Ai in i is ± 1). We find the same result if we instead apply principal component analysis and Bayesian model selection for the five choices of differential rotation parameter $Ai, i \in [1, 5]$ that we consider in this study.

While our simulations are numerically well converged, our tests reveal important systematic uncertainties associated with the nuclear EOS and the electron fraction Y_e in the inner core at bounce. We find that a $\pm 5\%$ variation of Y_e or a change of the EOS from Lattimer-Swesty with $K = 220\,{\rm MeV}$ [60] to the H. Shen EOS [59, 65] can both spoil the accuracy with which we can extract total and differential rotation, increasing the empirical errors by at least a factor of two even in the case of rapid core rotation and ideal source-detector alignment.

The EOS dependence of our results underlines the need for improved nuclear EOS tables that take into account all new experimental, observational, and theoretical EOS constraints [93]. Future simulations of rotating core collapse should also consider a broader range of nuclear EOS models (e.g., [94–96]) to further explore the sensitivity of the GW signal to the nuclear EOS.

Addressing uncertainties in the Y_e of the inner core will ultimately require full neutrino radiation-hydrodynamics simulations with up-to-date electron capture rates for heavy nuclei (e.g., [97]), full velocity dependence, and inelastic neutrino-electron scattering, which all have an effect on Y_e of the inner core (e.g., [98]). Such simulations, while computationally extremely intense, are possible now, for example with the radiation-hydrodynamic variant of the `CoCoNuT` code developed by B. Müller [99].

In this study, we have broken enirely new ground by combining precision computational waveform modeling with methods of gravitational wave astronomy. We have given the proof of principle that information on both total and differential rotation can be extracted, or at least constrained, from the GW signal of the next galactic core collapse event. Future work must address our study's many deficiencies. The most important of these may be: (*i*) Our simulations are 2D, making it impossible to study possibly important 3D features in the early postbounce GW signal [41–43]. (*ii*) We considered only a single rotation law, but realistic cores of massive stars do not necessarily follow it. (*iii*) We assumed optimal source–detector alignment and only a single detector with Gaussian noise. A real core collapse event is unlikely to be optimally aligned, but a network of second-generation detectors can mitigate reduced signal strength due to misalignment. (*iv*) Our treatment of electron capture during collapse relies on a single-parameter density fit of $Y_e(\rho)$ from spherically symmetric radiation-hydrodynamics simulations. Rapid rotation may lead to significant deviations from such simple fits in full 2D radiation-hydrodynamics simulations and this could have a significant quantitative effect on the predicted GW signals.

Acknowledgments

We thank P. Cerda-Duran, S. Couch, J. Clark, S. de Mink, B. Engels, R. Haas, I. S. Heng, H. Klion, J. Logue, P. Mösta, B. Müller, J. Novak, E. O'Connor, U. C. T. Gamma, C. Reisswig, L. Roberts, and A. Weinstein for helpful discussions. This work is supported by the National Science Foundation under grant numbers PHY-1151197, AST-1212170, OCI-0905046, and PHY-1068881, by the Sherman Fairchild Foundation, and the Alfred P. Sloan Foundation. Results presented in this article were obtained through computations on the Caltech computer cluster "Zwicky" (NSF MRI award No. PHY-0960291), on the NSF XSEDE network under grant TG-PHY100033, on machines of the Louisiana Optical Network Initiative, and at the National Energy Research Scientific Computing Center (NERSC), which is supported by the Office of Science of the US Department of Energy under contract DE-AC02-05CH11231.

TABLE II: Summary of simulation results. $\Omega_{\rm c}$ is the intitial central angular velocity, $\rho_{\rm c,b}$ is the central density at bounce, $\rho_{\rm c,pb}$ is the early postbounce central density, $\rho_{\rm max,pb}$ is the postbounce maximum density, $\beta_{\rm ic,b}$ and $\beta_{\rm ic,pb}$ ara ratios of the rotational kinetic energy to the gravitational binding energy of the inner core at bounce and early postbounce phase, respectively. $M_{\rm ic,b}$ and $J_{\rm ic,b}$ are the inner core mass and angular momentum at bounce, $|h_{+,2}|D$ is the second peak of the GW signal, while $|h_{+,\rm max}|D$ is its maximum value.

Model	$\Omega_{\rm c}$	$\rho_{\rm c,b}$	$\rho_{\rm c,pb}$	$\rho_{\rm max,pb}$	$\beta_{\rm ic,b}$	$\beta_{\rm ic,pb}$	$M_{\rm ic,b}$	$J_{\rm ic,b}$	HD	$\lvert h_{+,\rm max}\rvert D$
	[rad s^{-1}]	[10^{14}gcm^{-3}]	[10^{14}g cm^{-3}]	[10^{14}g cm^{-3}]	[10^{-2}]	[10^{-2}]	[$M_\odot$]	[10^{48}erg s]	[cm]	[cm]
A1O1	1.0	4.39	3.60	3.60	0.16	0.13	0.58	0.31	44.44	7.38
A1O1.5	1.5	4.38	3.59	3.59	0.36	0.30	0.58	0.46	44.53	15.30
A1O2	2.0	4.35	3.57	3.57	0.64	0.53	0.59	0.63	44.65	24.29
A1O2.5	2.5	4.36	3.55	3.55	1.00	0.82	0.58	0.77	44.81	39.67
A1O3	3.0	4.35	3.52	3.52	1.41	1.17	0.58	0.92	45.00	61.77
A1O3.5	3.5	4.32	3.49	3.49	1.90	1.58	0.59	1.11	45.23	83.27
A1O4	4.0	4.26	3.46	3.46	2.46	2.04	0.61	1.37	45.49	109.77
A1O4.5	4.5	4.22	3.42	3.42	3.07	2.54	0.61	1.50	45.80	138.94
A1O5	5.0	4.20	3.39	3.39	3.73	3.08	0.61	1.67	46.15	171.21
A1O5.5	5.5	4.15	3.34	3.35	4.45	3.66	0.65	1.99	46.54	207.07
A1O6	6.0	4.08	3.29	3.29	5.20	4.27	0.65	2.17	46.98	246.82
A1O6.5	6.5	4.03	3.24	3.25	6.01	4.92	0.65	2.39	47.47	291.49
A1O7	7.0	4.00	3.17	3.18	6.84	5.58	0.67	2.69	48.01	334.38
A1O7.5	7.5	3.92	3.11	3.12	7.73	6.28	0.68	2.94	48.60	374.54
A1O8	8.0	3.85	3.04	3.06	8.65	6.98	0.70	3.24	49.26	415.24
A1O8.5	8.5	3.74	2.97	3.00	9.60	7.70	0.70	3.50	49.98	452.12
A1O9	9.0	3.65	2.89	2.93	10.60	8.42	0.72	3.87	50.77	480.53
A1O9.5	9.5	3.56	2.81	2.85	11.50	9.14	0.74	4.17	51.64	502.39
A1O10	10.0	3.45	2.71	2.77	12.50	9.85	0.74	4.52	52.60	514.13
A1O10.5	10.5	3.35	2.62	2.69	13.40	10.57	0.76	4.92	53.66	520.96
A1O11	11.0	3.23	2.53	2.61	14.30	11.28	0.78	5.28	54.82	527.25
A1O11.5	11.5	3.14	2.48	2.55	15.20	12.02	0.79	5.71	56.13	535.99
A1O12	12.0	3.04	2.46	2.50	16.10	12.78	0.80	6.15	57.58	535.99
A1O12.5	12.5	3.00	2.41	2.44	17.00	13.57	0.82	6.63	59.21	532.98
A1O13	13.0	2.91	2.34	2.37	17.80	14.30	0.84	7.10	61.02	522.60
A1O13.5	13.5	2.82	2.25	2.28	18.50	14.96	0.85	7.58	-63.06	504.03
A1O13	14.0	2.72	2.15	2.18	19.20	15.55	0.86	8.06	65.37	476.98
A1O14.5	14.5	2.64	2.05	2.08	19.80	16.10	0.89	8.69	68.01	435.46
A1O15	15.0	2.53	1.89	1.92	20.30	16.41	0.91	9.33	71.01	393.11
A1O15.5	15.5	2.41	1.69	1.72	20.60	16.47	0.94	10.24	74.53	339.02
A2O1	1.0	4.42	3.59	3.59	0.36	0.31	0.57	0.44	0.98	16.12
A2O1.5	1.5	4.42	3.57	3.57	0.63	0.54	0.58	0.61	1.71	24.91
A2O2	2.0	4.31	3.54	3.55	1.10	0.95	0.58	0.81	3.01	45.35
A2O2.5	2.5	4.28	3.51	3.51	1.70	1.46	0.59	1.04	4.65	73.49
A2O3	3.0	4.26	3.48	3.48	2.42	2.06	0.61	1.31	6.60	104.90
A2O3.5	3.5	4.19	3.43	3.43	3.23	2.74	0.61	1.51	8.83	142.33
A2O4	4.0	4.14	3.38	3.39	4.14	3.49	0.63	1.86	11.32	182.76
A2O4.5	4.5	4.07	3.33	3.33	5.13	4.31	0.64	2.12	14.01	228.38
A2O5	5.0	4.00	3.26	3.26	6.18	5.18	0.65	2.46	16.89	278.38
A2O5.5	5.5	3.91	3.19	3.19	7.30	6.12	0.67	2.85	19.95	326.18
A2O6	6.0	3.80	3.11	3.12	8.48	7.08	0.70	3.25	23.17	369.89
A2O6.5	6.5	3.69	3.03	3.03	9.71	8.06	0.72	3.72	26.53	404.59
A2O7	7.0	3.58	2.93	2.94	10.96	9.03	0.72	4.09	29.94	425.35
A2O7.5	7.5	3.45	2.84	2.86	12.21	10.02	0.74	4.52	33.36	433.27
A2O8	8.0	3.30	2.73	2.75	13.40	10.95	0.76	5.00	-36.61	434.36
A2O8.5	8.5	3.17	2.63	2.65	14.55	11.88	0.78	5.63	-39.75	440.92
A2O9	9.0	3.04	2.52	2.54	15.65	12.80	0.80	6.35	-42.75	441.19
A2O9.5	9.5	2.88	2.44	2.45	16.73	13.80	0.82	6.90	-45.70	421.52
A2O10	10.0	2.77	2.33	2.34	17.70	14.70	0.84	7.62	-48.35	385.19
A2O10.5	10.5	2.65	2.19	2.20	18.58	15.55	0.86	8.37	50.76	327.00
A2O11	11.0	2.52	2.02	2.03	19.17	16.21	0.87	9.05	-52.37	283.57
A2O11.5	11.5	2.33	1.75	1.76	19.47	16.38	0.89	9.76	-53.19	245.87
A3O1	1.0	4.47	3.59	3.59	0.36	0.31	0.57	0.45	44.59	15.84
A3O1.5	1.5	4.38	3.56	3.57	0.80	0.70	0.58	0.69	44.87	32.13

Continued on Next page...

TABLE II: Continued

Model	$\Omega_{\rm c}$ [rad s^{-1}]	$\rho_{\rm c,b}$ [10^{14}gcm^{-3}]	$\rho_{\rm c,pb}$ [10^{14}g cm^{-3}]	$\rho_{\rm max,pb}$ [10^{14}g cm^{-3}]	$\beta_{\rm ic,b}$ [10^{-2}]	$\beta_{\rm ic,pb}$ [10^{-2}]	$M_{\rm ic,b}$ [$M_\odot$]	$J_{\rm ic,b}$ [10^{48}erg s]	HD [cm]	$\lvert h_{+,\rm max}\rvert D$ [cm]
A3O2	2.0	4.26	3.53	3.53	1.40	1.23	0.59	0.94	45.27	60.87
A3O2.5	2.5	4.27	3.49	3.50	2.15	1.88	0.61	1.24	45.79	94.90
A3O3	3.0	4.15	3.45	3.45	3.03	2.63	0.60	1.45	46.44	135.69
A3O3.5	3.5	4.12	3.40	3.40	4.04	3.48	0.63	1.82	47.26	178.53
A3O4	4.0	4.04	3.33	3.33	5.14	4.41	0.65	2.18	48.25	227.84
A3O4.5	4.5	3.96	3.27	3.27	6.32	5.42	0.66	2.55	49.44	274.55
A3O5	5.0	3.85	3.18	3.18	7.56	6.48	0.68	2.98	50.88	317.99
A3O5.5	5.5	3.74	3.09	3.10	8.87	7.59	0.70	3.40	52.60	358.69
A3O6	6.0	3.62	3.00	3.00	10.20	8.70	0.71	3.81	54.70	381.64
A3O6.5	6.5	3.49	2.89	2.90	11.60	9.80	0.73	4.40	57.28	391.75
A3O7	7.0	3.34	2.79	2.80	12.90	10.88	0.75	4.92	-60.51	402.40
A3O7.5	7.5	3.18	2.66	2.67	14.10	11.86	0.77	5.60	-64.66	406.50
A3O8	8.0	3.04	2.55	2.56	15.30	12.90	0.79	6.31	-70.24	397.21
A3O8.5	8.5	2.90	2.44	2.45	16.40	13.96	0.81	7.02	-78.19	370.71
A3O9	9.0	2.75	2.31	2.32	17.40	14.94	0.83	7.74	-90.70	319.63
A3O9.5	9.5	2.57	2.16	2.16	18.20	15.87	0.85	8.61	-112.97	258.16
A4O1	1.0	4.36	3.58	3.58	0.47	0.42	0.57	0.51	1.27	18.49
A4O1.5	1.5	4.31	3.55	3.55	1.03	0.95	0.58	0.78	2.82	43.16
A4O2	2.0	4.26	3.51	3.51	1.80	1.65	0.60	1.10	4.91	80.59
A4O2.5	2.5	4.16	3.46	3.46	2.74	2.48	0.60	1.35	7.49	123.48
A4O3	3.0	4.11	3.41	3.41	3.84	3.43	0.63	1.75	10.49	169.65
A4O3.5	3.5	4.03	3.33	3.33	5.05	4.49	0.64	2.12	13.80	218.27
A4O4	4.0	3.92	3.26	3.26	6.34	5.65	0.66	2.53	17.33	262.80
A4O4.5	4.5	3.80	3.17	3.17	7.71	6.86	0.67	2.90	21.05	302.96
A4O5	5.0	3.69	3.06	3.07	9.12	8.07	0.70	3.46	24.91	330.28
A4O5.5	5.5	3.54	2.97	2.97	10.57	9.30	0.72	4.05	28.88	345.31
A4O6	6.0	3.39	2.86	2.86	11.94	10.47	0.73	4.56	-32.62	360.06
A4O6.5	6.5	3.26	2.74	2.74	13.15	11.51	0.75	5.20	-35.92	362.52
A5O1	1.0	4.36	3.58	3.58	0.52	0.48	0.58	0.54	44.92	22.67
A5O1.5	1.5	4.31	3.54	3.55	1.13	1.07	0.58	0.81	45.64	52.18
A5O2	2.0	4.20	3.50	3.50	1.97	1.84	0.60	1.14	46.71	88.98
A5O2.5	2.5	4.16	3.45	3.45	2.99	2.75	0.61	1.42	48.21	133.40
A5O3	3.0	4.08	3.39	3.39	4.15	3.77	0.63	1.57	50.29	183.31
A5O3.5	3.5	3.99	3.31	3.31	5.42	4.90	0.64	2.18	53.19	229.20
A5O4	4.0	3.87	3.24	3.24	6.74	6.10	0.67	2.67	57.43	270.92
A5O4.5	4.5	3.74	3.15	3.15	8.12	7.32	0.68	3.12	64.16	303.24
A5O5	5.0	3.64	3.06	3.06	9.45	8.49	0.70	3.61	77.44	328.64
A5O5.5	5.5	3.53	2.96	2.96	10.70	9.54	0.71	4.05	161.22	333.56

TABLE III: Sumary of properties of models for injection. $\Omega_{\rm c}$ is the intitial central angular velocity, $\rho_{\rm c,b}$ is the central density at bounce, $\rho_{\rm c,pb}$ is the early postbounce central density, $\rho_{\rm max,pb}$ is the postbounce maximum density, $\beta_{\rm ic,b}$ and $\beta_{\rm ic,pb}$ ara ratios of the rotational kinetic energy to the gravitational binding energy of the inner core at bounce and early postbounce phase, respectively. $M_{\rm ic,b}$ and $J_{\rm ic,b}$ are the inner core mass and angular momentum at bounce, $|h_{+,2}|D$ is the second peak of the GW signal, while $|h_{+,\rm max}|D$ is its maximum value.

Model	$\Omega_{\rm c}$ [rad s^{-1}]	$\rho_{\rm c,b}$ [10^{14}gcm^{-3}]	$\rho_{\rm c,pb}$ [10^{14}g cm^{-3}]	$\rho_{\rm max,pb}$ [10^{14}g cm^{-3}]	$\beta_{\rm ic,b}$ [10^{-2}]	$\beta_{\rm ic,pb}$ [10^{-2}]	$M_{\rm ic,b}$ [$M_\odot$]	$J_{\rm ic,b}$ [10^{48}erg s]	HD [cm]	$\lvert h_{+,\rm max}\rvert D$ [cm]
A1O5.25	5.25	4.28	3.37	3.37	4.09	3.36	0.63	1.58	111.19	189.59
A1O5.25m	5.25	4.18	3.41	3.41	4.04	3.38	0.60	1.50	93.98	163.91
A1O5.25p	5.25	4.18	3.30	3.30	4.14	3.33	0.60	1.50	132.49	213.63
A1O5.25s	5.25	3.33	2.65	2.65	3.79	3.15	0.60	1.51	87.97	158.17
A1O8.25	8.25	3.87	3.00	3.03	9.12	7.33	0.68	1.77	252.70	436.55
A1O8.25m	8.25	3.88	3.05	3.08	9.02	7.37	0.68	1.70	191.78	377.27
A1O8.25p	8.25	3.88	2.94	2.96	9.19	7.29	0.68	1.70	302.69	469.06
A1O8.25s	8.25	2.98	2.45	2.45	8.46	6.87	0.66	1.66	218.82	368.80
A1O10.25	10.25	3.42	2.65	2.72	12.90	10.20	0.76	1.90	199.43	521.24
A1O10.25m	10.25	3.45	2.75	2.80	12.80	10.20	0.74	1.86	180.30	490.37

Continued on Next page...

TABLE III: Continued

Model	$\Omega_{\rm c}$ [rad s^{-1}]	$\rho_{\rm c,b}$ [10^{14}gcm^{-3}]	$\rho_{\rm c,pb}$ [10^{14}g cm^{-3}]	$\rho_{\rm max,pb}$ [10^{14}g cm^{-3}]	$\beta_{\rm ic,b}$ [10^{-2}]	$\beta_{\rm ic,pb}$ [10^{-2}]	$M_{\rm ic,b}$ [$M_\odot$]	$J_{\rm ic,b}$ [10^{48}erg s]	HD [cm]	$\lvert h_{+,\rm max}\rvert D$ [cm]
A1O10.25p	10.25	3.45	2.59	2.65	13.00	10.10	0.74	1.86	228.11	540.91
A1O10.25s	10.25	2.76	2.22	2.26	12.20	9.64	0.72	1.81	211.99	492.01
A1O12.25	12.25	3.06	2.44	2.47	16.60	13.10	0.81	2.03	202.70	541.45
A1O12.25m	12.25	3.06	2.49	2.53	16.50	13.20	0.80	2.00	177.02	559.48
A1O12.25p	12.25	3.06	2.33	2.36	16.40	13.00	0.80	2.00	174.29	512.50
A1O12.25s	12.25	2.51	1.97	2.05	15.90	12.50	0.77	1.93	-171.29	522.33
A1O13.75	13.75	2.83	2.22	2.25	18.90	15.40	0.83	2.06	168.01	492.28
A1O13.75m	13.75	2.88	2.32	2.35	19.10	15.50	0.85	2.13	182.76	547.19
A1O13.75p	13.75	2.88	1.94	1.97	18.30	14.40	0.85	2.13	129.49	398.03
A1O13.75s	13.75	2.36	1.89	1.92	18.40	14.70	0.81	2.02	158.99	511.13
A1O15.25	15.25	2.49	1.79	1.82	20.40	16.50	0.88	2.19	94.80	369.07
A1O15.25m	15.25	2.61	2.06	2.10	21.10	17.60	0.89	2.22	160.36	469.33
A1O15.25p	15.25	1.14	1.16	2.10	19.40	14.50	0.89	2.22	-59.28	262.53
A1O15.25s	15.25	2.28	1.65	1.70	20.50	16.40	0.85	2.13	123.21	469.88

APPENDIX A: $Y_e(\rho)$ PARAMETRIZED DELEPTONIZATION SCHEME

Following [75], we use the following fitting function to model the functional dependence of $Y_{\rm e}$ on ρ:

$$Y_{\rm e} = \frac{1}{2}\left(Y_{\rm e,1}+Y_{\rm e,1}\right)+\frac{x}{2}\left(Y_{\rm e,1}-Y_{\rm e,1}\right) + Y_{\rm e,c}\left[1-|x|+4|x|(|x|-1/2)(|x|-1)\right], \quad \text{(A1)}$$

where

$$x=\max\left[-1,\min\left(1,\frac{2\log\rho-\log\rho_2-\log\rho_1}{\log\rho_2-\log\rho_1}\right)\right] \quad \text{(A2)}$$

and $\rho_1 = 10^7\,{\rm g\,cm^{-3}}$, $\rho_2 = 10^{13}\,{\rm g\,cm^{-3}}$, $Y_{\rm e,1} = 0.5$, $Y_{\rm e,2} = 0.29$, and $Y_{\rm e,c} = 0.035$. When density ρ is above ρ_2, we make the following correction to $Y_{\rm e}$:

$$Y_{\rm e} = Y_{\rm e}(\rho_2)+\frac{\log\rho-\log\rho_2}{\log\rho_{\rm cor}-\log\rho_2}\left[Y_{\rm e,cor}-Y_{\rm e}(\rho_2)\right], \quad \text{(A3)}$$

where $Y_{\rm e,cor}$ is chosen to be 0.2717 for our fiducial $Y_{\rm e}(\rho)$ parametrization. In our 5 % reduced (increased) $Y_{\rm e}(\rho)$ parametrization, we use 5 % smaller (larger) value of $Y_{\rm e,cor}$.

[1] H. Dimmelmeier, J. A. Font, and E. Müller, Astron. Astrophys. **393**, 523 (2002).
[2] D. Shoemaker, Tech. Rep. LIGO-T0900288-v3, LIGO Scientific Collaboration (2010), URL https://dcc.ligo.org/cgi-bin/DocDB/ShowDocument?docid=t0900288.
[3] E. Abdikamalov, S. Gossan, A. M. DeMaio, and C. D. Ott, Unpublished manuscript. (2013.).
[4] H. A. Bethe, Rev. Mod. Phys. **62**, 801 (1990).
[5] H. A. Bethe and J. R. Wilson, Astrophys. J. **295**, 14 (1985).
[6] H.-T. Janka, F. Hanke, L. Hüdepohl, A. Marek, B. Müller, and M. Obergaulinger, Prog. Th. Exp. Phys. **2012**, 01A309 (2012).
[7] A. Burrows, Rev. Mod. Phys. **85**, 245 (2013).
[8] J. M. Blondin, A. Mezzacappa, and C. DeMarino, Astrophys. J. **584**, 971 (2003).
[9] S. W. Bruenn, A. Mezzacappa, W. R. Hix, E. J. Lentz, O. E. Bronson Messer, E. J. Lingerfelt, J. M. Blondin, E. Endeve, P. Marronetti, and K. N. Yakunin, Astrophys. J. Lett. **767**, L6 (2013).
[10] B. Müller, H.-T. Janka, and A. Marek, Astrophys. J. **756**, 84 (2012).
[11] B. Müller, H.-T. Janka, and A. Heger, Astrophys. J. **761**, 72 (2012).
[12] F. Hanke, B. Müller, A. Wongwathanarat, A. Marek, and H.-T. Janka, Astrophys. J. **770**, 66 (2013).
[13] T. Takiwaki, K. Kotake, and Y. Suwa, Submitted to the Astrophys. J. Lett.; arXiv:1308.5755 (2013).
[14] M. R. Drout, A. M. Soderberg, A. Gal-Yam, S. B. Cenko, D. B. Fox, D. C. Leonard, D. J. Sand, D.-S. Moon, I. Arcavi, and Y. Green, Astrophys. J. **741**, 97 (2011).
[15] N. Smith, W. Li, A. V. Filippenko, and R. Chornock, Mon. Not. Roy. Astron. Soc. **412**, 1522 (2011).
[16] M. T. Botticella, C. Trundle, A. Pastorello, S. Rodney, A. Rest, S. Gezari, S. J. Smartt, G. Narayan, M. E. Huber, J. L. Tonry, et al., Astrophys. J. Lett. **717**, L52 (2010).
[17] N. Smith, S. B. Cenko, N. Butler, J. S. Bloom, M. M. Kasliwal, A. Horesh, S. R. Kulkarni, N. M. Law, P. E. Nugent, E. O. Ofek, et al., Mon. Not. Roy. Astron. Soc. **420**, 1135 (2012).
[18] M. Modjaz, Astron. Nachr. **332**, 434 (2011).
[19] J. Hjorth and J. S. Bloom, in *Gamma-Ray Bursts*, edited by C. Kouveliotou, R. A. M. J. Wijers, and S. E. Woosley (Cambridge University Press, Cambridge, UK, 2011).
[20] G. S. Bisnovatyi-Kogan, Astron. Zh. **47**, 813 (1970).
[21] J. M. LeBlanc and J. R. Wilson, Astrophys. J. **161**, 541 (1970).
[22] J. C. Wheeler, I. Yi, P. Höflich, and L. Wang, Astrophys. J. **537**, 810 (2000).
[23] J. C. Wheeler, D. L. Meier, and J. R. Wilson, Astrophys.

J. **568**, 807 (2002).
[24] A. Burrows, L. Dessart, E. Livne, C. D. Ott, and J. Murphy, Astrophys. J. **664**, 416 (2007).
[25] S. E. Woosley and J. S. Bloom, Ann. Rev. Astron. Astrophys. **44**, 507 (2006).
[26] B. D. Metzger, D. Giannios, T. A. Thompson, N. Bucciantini, and E. Quataert, Mon. Not. Roy. Astron. Soc. **413**, 2031 (2011).
[27] A. Heger, S. E. Woosley, and H. C. Spruit, Astrophys. J. **626**, 350 (2005).
[28] C. D. Ott, A. Burrows, T. A. Thompson, E. Livne, and R. Walder, Astrophys. J. Suppl. Ser. **164**, 130 (2006).
[29] S. E. Woosley and A. Heger, Astrophys. J. **637**, 914 (2006).
[30] S.-C. Yoon, N. Langer, and C. Norman, Astron. Astrophys. **460**, 199 (2006).
[31] S. E. de Mink, N. Langer, R. G. Izzard, H. Sana, and A. de Koter, Astrophys. J. **764**, 166 (2013).
[32] L. Dessart, E. O'Connor, and C. D. Ott, Astrophys. J. **754**, 76 (2012).
[33] S. A. Balbus and J. F. Hawley, Astrophys. J. **376**, 214 (1991).
[34] M. Obergaulinger, P. Cerdá-Durán, E. Müller, and M. A. Aloy, Astron. Astrophys. **498**, 241 (2009).
[35] S. Akiyama, J. C. Wheeler, D. L. Meier, and I. Lichtenstadt, Astrophys. J. **584**, 954 (2003).
[36] T. A. Thompson, E. Quataert, and A. Burrows, Astrophys. J. **620**, 861 (2005).
[37] T. K. Suzuki, K. Sumiyoshi, and S. Yamada, Astrophys. J. **678**, 1200 (2008).
[38] H. Dimmelmeier, C. D. Ott, A. Marek, and H.-T. Janka, Phys. Rev. D. **78**, 064056 (2008).
[39] C. D. Ott, E. Abdikamalov, E. O'Connor, C. Reisswig, R. Haas, P. Kalmus, S. Drasco, A. Burrows, and E. Schnetter, Phys. Rev. D. **86**, 024026 (2012).
[40] E. B. Abdikamalov, C. D. Ott, L. Rezzolla, L. Dessart, H. Dimmelmeier, A. Marek, and H. Janka, Phys. Rev. D. **81**, 044012 (2010).
[41] C. D. Ott, H. Dimmelmeier, A. Marek, H.-T. Janka, I. Hawke, B. Zink, and E. Schnetter, Phys. Rev. Lett. **98**, 261101 (2007).
[42] S. Scheidegger, R. Käppeli, S. C. Whitehouse, T. Fischer, and M. Liebendörfer, Astron. Astrophys. **514**, A51 (2010).
[43] T. Kuroda, T. Takiwaki, and K. Kotake, Submitted to Phys. Rev. D., arXiv:1304.4372 (2013).
[44] E. Müller, Astron. Astrophys. **114**, 53 (1982).
[45] R. Mönchmeyer, G. Schäfer, E. Müller, and R. Kates, Astron. Astrophys. **246**, 417 (1991).
[46] S. Yamada and K. Sato, Astrophys. J. **450**, 245 (1995).
[47] T. Zwerger and E. Müller, Astron. Astrophys. **320**, 209 (1997).
[48] K. Kotake, S. Yamada, and K. Sato, Phys. Rev. D. **68**, 044023 (2003).
[49] M. Shibata and Y. Sekiguchi, Phys. Rev. D **69**, 084024 (2004).
[50] C. D. Ott, A. Burrows, E. Livne, and R. Walder, Astrophys. J. **600**, 834 (2004).
[51] C. D. Ott, H. Dimmelmeier, A. Marek, H.-T. Janka, B. Zink, I. Hawke, and E. Schnetter, Class. Quantum Grav. **24**, 139 (2007).
[52] H. Dimmelmeier, C. D. Ott, H.-T. Janka, A. Marek, and E. Müller, Phys. Rev. Lett. **98**, 251101 (2007).
[53] T. Takiwaki and K. Kotake, Astrophys. J. **743**, 30 (2011).
[54] K. Kotake, S. Yamada, K. Sato, K. Sumiyoshi, H. Ono, and H. Suzuki, Phys. Rev. D. **69**, 124004 (2004).
[55] M. Obergaulinger, M. A. Aloy, and E. Müller, Astron. Astrophys. **450**, 1107 (2006).
[56] M. Obergaulinger, M. A. Aloy, H. Dimmelmeier, and E. Müller, Astron. Astrophys. **457**, 209 (2006).
[57] M. Shibata, Y. T. Liu, S. L. Shapiro, and B. C. Stephens, Phys. Rev. D. **74**, 104026 (2006).
[58] H. Shen, H. Toki, K. Oyamatsu, and K. Sumiyoshi, Prog. Th. Phys. **100**, 1013 (1998).
[59] H. Shen, H. Toki, K. Oyamatsu, and K. Sumiyoshi, Astrophys. J. Supp. Ser. **197**, 20 (2011).
[60] J. M. Lattimer and F. D. Swesty, Nucl. Phys. A **535**, 331 (1991).
[61] H. Dimmelmeier, J. A. Font, and E. Müller, Astron. Astrophys. **388**, 917 (2002).
[62] H. Dimmelmeier, J. Novak, J. A. Font, J. M. Ibáñez, and E. Müller, Phys. Rev. D. **71**, 064023 (2005).
[63] M. Liebendörfer, M. Rampp, H.-T. Janka, and A. Mezzacappa, Astrophys. J. **620**, 840 (2005).
[64] S. E. Woosley and A. Heger, Phys. Rep. **442**, 269 (2007).
[65] H. Shen, H. Toki, K. Oyamatsu, and K. Sumiyoshi, Nucl. Phys. A **637**, 435 (1998), URL `http://user.numazu-ct.ac.jp/$\sim$sumi/eos`.
[66] J. Logue, C. D. Ott, I. S. Heng, P. Kalmus, and J. Scargill, Phys. Rev. D. **86**, 044023 (2012).
[67] G. M. Harry (for the LIGO Scientific Collaboration), Class. Quantum Grav. **27**, 084006 (2010).
[68] J. A. Font, Liv. Rev. Rel. **11**, 7 (2008).
[69] P. Colella and P. R. Woodward, J. Comp. Phys. **54**, 174 (1984).
[70] B. Einfeldt, in *Shock tubes and waves; Proceedings of the Sixteenth International Symposium, Aachen, Germany, July 26–31, 1987. VCH Verlag, Weinheim, Germany* (1988), p. 671.
[71] E. O'Connor and C. D. Ott, Class. Quantum Grav. **27**, 114103 (2010).
[72] `stellarcollapse.org`: A Community Portal for Stellar Collapse, Core-Collapse Supernova and GRB Simulations., URL `http://www.stellarcollapse.org`.
[73] E. O'Connor and C. D. Ott, Astrophys. J. **730**, 70 (2011).
[74] E. O'Connor and C. D. Ott, in *11th Symposium on Nuclei in the Cosmos, July 19–23, 2010, Heidelberg, Germany* (2010), Proceedings of Science, p. 154.
[75] M. Liebendörfer, Astrophys. J. **633**, 1042 (2005).
[76] C. D. Ott, E. Abdikamalov, P. Mösta, R. Haas, S. Drasco, E. P. O'Connor, C. Reisswig, C. A. Meakin, and E. Schnetter, Astrophys. J. **768**, 115 (2013).
[77] C. Reisswig, C. D. Ott, U. Sperhake, and E. Schnetter, Phys. Rev. D. **83**, 064008 (2011).
[78] A. Heger, N. Langer, and S. E. Woosley, Astrophys. J. **528**, 368 (2000).
[79] H. C. Spruit, Astron. Astrophys. **381**, 923 (2002).
[80] N. Langer, Ann. Rev. Astron. Astroph. **50**, 107 (2012).
[81] J. L. Friedman, L. Parker, and J. R. Ipser, Astrophys. J. **304**, 115 (1986).
[82] J. E. Tohline, Astrophys. J. **285**, 721 (1984).
[83] L. S. Shapiro and S. A. Teukolsky, *Black Holes, White Dwarfs and Neutron Stars* (John Wiley & Sons, New York U. S. A., 1983).
[84] K. Hayama, S. Desai, K. Kotake, S. D. Mohanty, M. Rakhmanov, T. Summerscales, and S. Yoshida, Classical and Quantum Gravity **25**, 184022 (2008).
[85] C. W. Helstrom, *Statistical Theory of Signal Detection*

(Pergamon Press, 1968), Second ed.
[86] K. V. Mardia, J. T. Kent, and J. M. Bibby, *Multivariate Analysis* (Academic Press, 1980).
[87] C. Röver, M. Bizouard, N. Christensen, H. Dimmelmeier, I. S. Heng, and R. Meyer, Phys. Rev. D. **80**, 102004 (2009).
[88] J. Skilling, in *AIP Conference Proceedings: 24th International Workshop on Bayesian Inference and Maximum Entropy Methods in Science and Engineering,*, edited by R. Fischer, R. Preuss, & U. V. Toussaint (2004), vol. 735, p. 395.
[89] O. H. Ramírez-Agudelo, S. Simón-Díaz, H. Sana, A. de Koter, C. Sabín-Sanjulían, S. E. de Mink, P. L. Dufton, G. Gräfener, C. J. Evans, A. Herrero, et al., Accepted for publication in Astron. Astrophys.; arXiv:1309.2929 (2013).
[90] W. Huang, D. R. Gies, and M. V. McSwain, Astrophys. J. **722**, 605 (2010).
[91] P. Goldreich and S. V. Weber, Astrophys. J. **238**, 991 (1980).
[92] A. Yahil, Astrophys. J. **265**, 1047 (1983).
[93] J. M. Lattimer and Y. Lim, Astrophys. J. **771**, 51 (2013).
[94] G. Shen, C. J. Horowitz, and S. Teige, Phys. Rev. C **83**, 035802 (2011).
[95] G. Shen, C. J. Horowitz, and E. O'Connor, Phys. Rev. C **83**, 065808 (2011).
[96] A. W. Steiner, M. Hempel, and T. Fischer, Astrophys. J. **774**, 17 (2013).
[97] A. Juodagalvis, K. Langanke, W. R. Hix, G. Martínez-Pinedo, and J. M. Sampaio, Nuc. Phys. A **848**, 454 (2010).
[98] E. J. Lentz, A. Mezzacappa, O. E. Bronson Messer, M. Liebendörfer, W. R. Hix, and S. W. Bruenn, Astrophys. J. **747**, 73 (2012).
[99] B. Müller, Ph.D. thesis, Technische Universität München, München, Germany (2009).